UC-90d
LBL-7604
c.1

CORROSION OF IRON-BASE ALLOYS BY COAL CHAR AT 871° AND 982° C

Bruce Abbott Gordon
(M. S. thesis)

March 1978

Prepared for the U. S. Department of Energy
under Contract W-7405-ENG-48

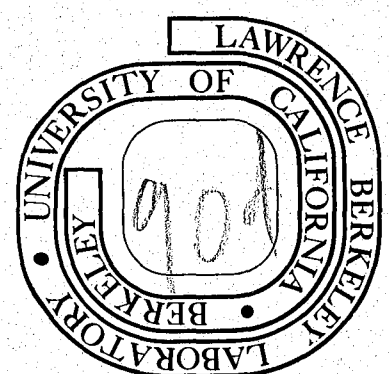

LBL-7604
c.1

LBL-7604

Corrosion of Iron-Base Alloys by Coal Char at 871° and 982°C

by

Bruce Abbott Gordon
Materials and Molecular Research Division, Lawrence Berkeley Laboratory
and Department of Chemical Engineering, University of California,
Berkeley, California 94720

Abstract

The high pressures and temperatures required for the processing of coal lead to accelerated corrosion of gasifier components by oxygen and sulfur present in the gas phase. Coal char, the solid byproduct of coal processing, contains sufficient inorganic sulfur to result in internal attack of the alloys composing the gasifier components.

The role of coal char in coal processing and of thermodynamics in gas phase corrosion are discussed.

Experiments are performed to determine whether $CaSO_4$ or FeS are responsible for the internal attack on Fe-Cr-Al and Fe-Cr-Ni alloys observed under conditions of both high oxygen partial pressure and 982°C and low oxygen partial pressure and 982°C. Exposure at 871°C resulted in virtually no attack from coal char and FeS and very slight attack from $CaSO_4$. The morphologies and rates of attack indicate that at low oxygen partial pressures (about 10^{-19} atmosphere) the presence of $CaSO_4$ can result in internal sulfidation whereas at high oxygen partial pressures (about 10^{-15} atmosphere), the presence of FeS can result in internal sulfidation. Comparison of these results with those actually observed from coal char at 982°C indicate that FeS is primarily responsible for attack by coal char but that $CaSO_4$ can also result in such attack although the overall mechanism and rate of attack may be different.

TABLE OF CONTENTS

INTRODUCTION

The United States is in the middle of an energy crisis. It is not confined to the United States, but, as this country is the most industrialized country in the world, its impact will be felt here first. The world is running out of petroleum and natural gas, and there is no way to prevent it. The United States is quite fortunate in that it is not totally dependent on foreign oil for its industry. This, however, is only a temporary situation. Eventually we too will run out of easily accessible petroleum and will have to rely on more expensive forms of energy. This country does have an abundance of another kind of fossil fuel that can be processed into petroleum-type products: coal. We have sufficient coal reserves to last us at least 200 years, enough time to develop other forms of energy to supplement and supplant fossil fuels.

Coal, like petroleum, is an attractive fuel largely because of its high energy/unit volume ratio. Unlike petroleum, it is not easy to process because it is a solid nor is it environmentally as attractive because of its high mineral content. In processing plants this shows up as ash, slag, and char. All of these must be removed and disposed of during the operation of the plant. Ash is the result of combustion and consists of the non-combustible constituents of the coal: SiO_2, Al_2O_3, FeO, other metallic oxides and other compounds such as $CaSO_4$ and $MgSO_4$. Slag is the result of high-temperature processing and consists of those processing byproducts that have liquefied and sintered at the high temperatures of the processing operation (around 1000°C). It is mostly sintered oxides and unprocessed carbon mixed with relatively

low-melting metallic sulfides and sulfates. Char is the solid byproduct of coal-processing. Besides the uncombustible oxides, it contains considerable residual carbon plus inorganic sulfides and sulfates. The purpose of this research is to examine the role of coal char and its constituents in the corrosion of iron-base alloys.

CHAPTER 1

Coal Processing and Coal Char

A. The Energy Crisis

The energy crisis is a fact that will be with us as long as we live. We have sufficient energy available in a compact form to meet our needs, but availing ourselves of this energy is an involved process. Since the Second World War, this country has enjoyed an upsurge in industrial output that has never before been seen. As a result of this, the United States, with 1/16th of the world's population, uses 1/3rd of the world's total energy output (1). Energy use is increasing at the rate of seven percent a year (2), and with it goes an accelerated depletion of known oil and natural gas reserves. The dependence on foreign sources of oil is likewise increasing but more rapidly. In 1948 the U.S. was a net exporter of energy (coal and oil) (1), but by 1973 over 30% of the total petroleum supplies depended upon foreign imports (3). The combination of increasing reliance on foreign imports and decreasing domestic supplies (see Figure 1) makes it imperative that alternate forms of energy be found and efficiently exploited.

The U.S. has abundant coal resources, enough to meet all U.S. energy requirements for hundreds of years. Table 1 gives a breakdown of available vs. currently recoverable reserves. It is abundantly clear that, even using only those reserves recoverable by current techniques and under current mining and environmental restrictions, the U.S. has sufficient reserves of fossil energy for all its needs for many years.

Coal is an inconvenient form of fossil fuel. It can't be pumped through pipes, it doesn't combust cleanly, and it leaves considerable

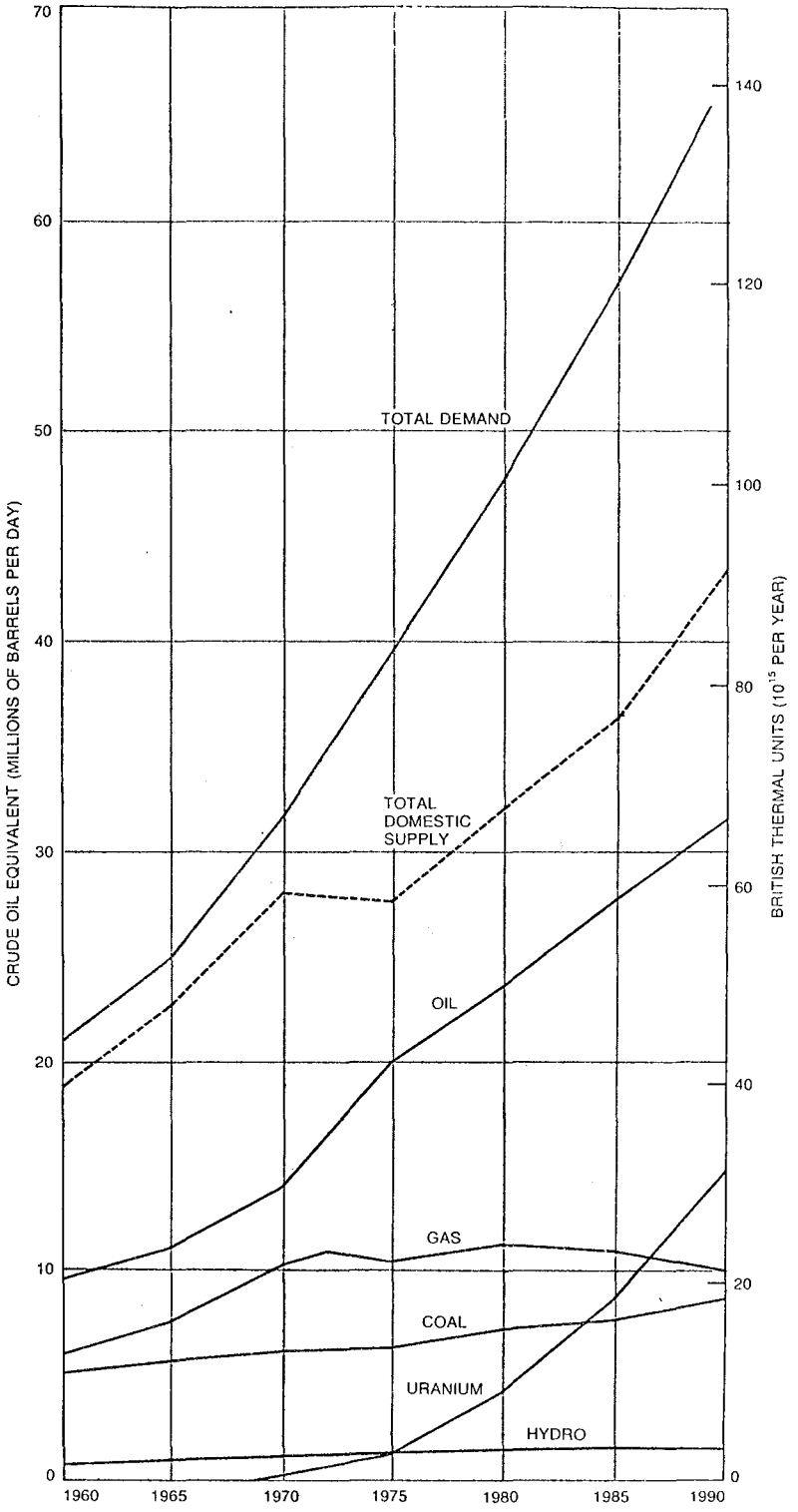

Figure 1. Demand and supply. This represents a breakdown of the total domestic energy supply. Note in particular how much faster demand is rising than supply and the relatively small role coal plays in the current energy picture.

Table 1. Comparison of mapped and economically available coal reserves to total estimated reserves (3).

	billion tons	
Remaining measured and indicated reserves (2)	349.1	
Economically available reserves	209.2	
Recoverable reserves (1)	104.6	
Mapped and explored reserves (3)	1,581	4,805 total
Unmapped and unexplored	3,224	

(1) Based on 50% recovery of economically available reserves.

(2) Only includes that portion of (3) that is actually available to resource bank.

residue. If the environmental impact of a large strip mine was not sufficient proof that coal is a largely undesirable fuel, the scrubbing and processing that are required of combustion waste gases and ash are. Coal can be processed, however, into a suitable form for clean combustion and chemical processing.

B. Coal Processing

Conversion of coal to synthetic fossil fuels has been around for quite a while. Germany, cut off from its foreign sources of oil during World War II, was producing all of its aircraft fuel from coal during the latter stages of the war. The technology used has been known since the 1930's but has been updated for use in, for example, the Lurgi process (4). This is a low pressure (28 atmospheres), low temperature (500°C) process that produces a low-BTU (about 500-600 BTU/scf or 19-22 MJ/m^3) synthetic natural gas (SNG). The gasifiers are all small, and a large number must be used to produce a sufficient amount of SNG.

Research in the U.S. has produced a variety of gasification processes, several of which have been or are being scaled up into pilot plants. The Synthane process, developed by the U.S. Bureau of Mines Pittsburgh Energy Research Center, is a case in point (5).

Figure 2 shows the overall commercial Synthane SNG process. The coal is pulverized and pretreated with steam at about 400°C to prevent agglomeration. It is then sent to the gasifier where it is mixed with steam and oxygen at about 950°-1000°C. This produces a complex gas mixture (see Table 2) containing mostly hydrogen, CO , CO_2 , H_2O , and CH_4 with traces of H_2S . This is the raw synthesis gas which is

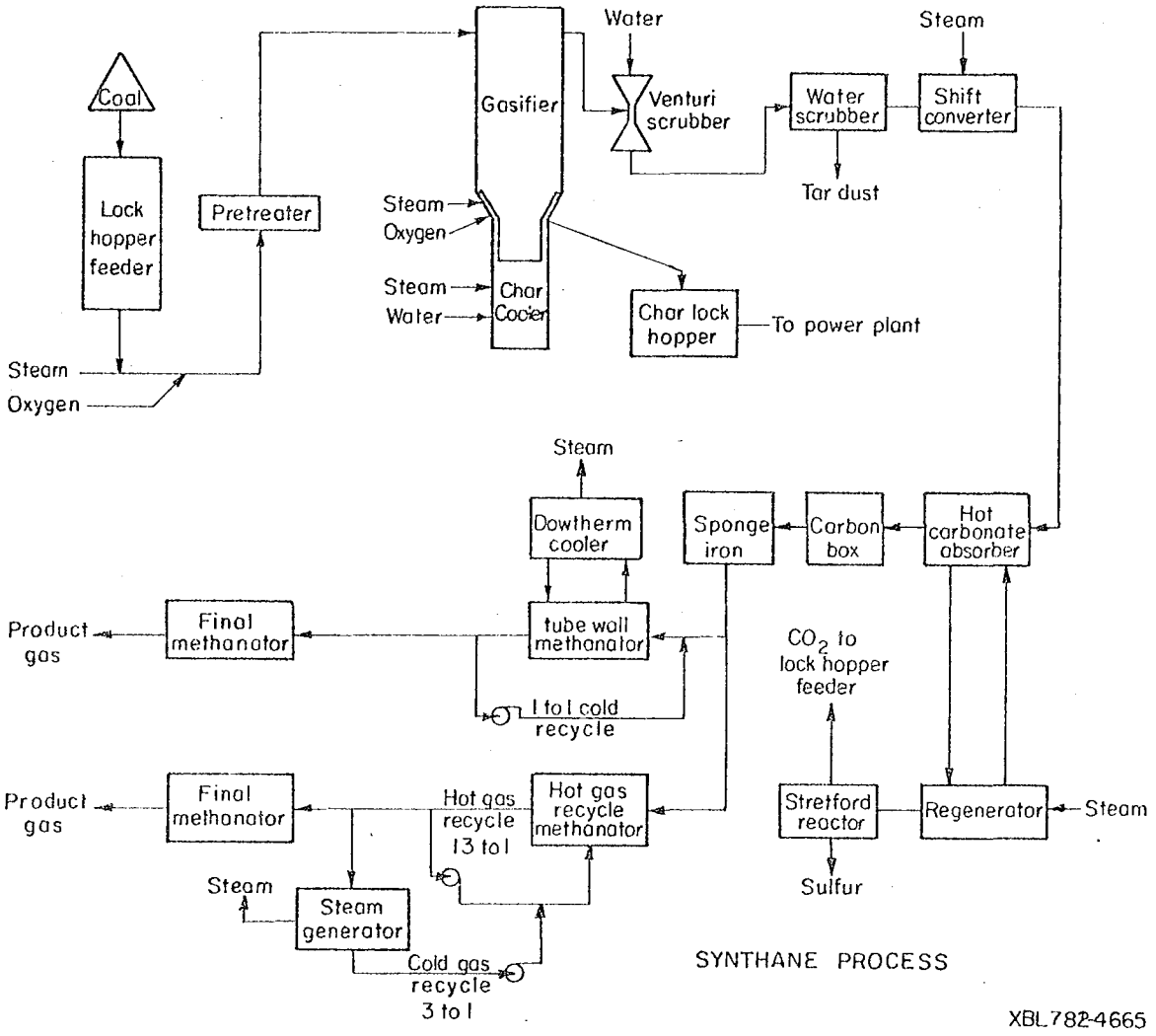

Figure 2. Process flow diagram for Synthane Process SNG plant.

Table 2. Ranges of component concentrations in coal gasifiers operating between 871°C and 982°C (1600°F-1800°F)(13).

Component	Range (mole %)
H_2	15-50
H_2O	15-40
CO_2	4-20
CO	5-15
CH_4	8-20
H_2S	0.03-1.0

scrubbed to remove the particulate matter and sent to the shift converter. The shift converter produces CO_2 and H_2 via the reaction

$$CO + H_2O \rightleftarrows CO_2 + H_2 \ . \qquad (1\text{-}1)$$

This provides sufficient hydrogen for catalytic methanation of the remaining carbon monoxide:

$$CO + 3H_2 \rightleftarrows CH_4 + H_2O \ . \qquad (1\text{-}2)$$

After this final methanation step, the gas is cooled, cleaned, and shipped out.

The unprocessed particulate matter is called char. It contains considerable fixed carbon (see Table 3 (6)) and can be burned in a boiler to generate steam and heat for the endothermic reactions above as well as for electrical power.

C. Corrosion

Table 2 shows the typical compositions of the raw synthesis gas from a second-generation SNG plant. The analysis is taken after the gas exits from the gasifier and has been quenched to a temperature low enough to permit handling and analysis. This occurs rapidly enough that these composition ranges still hold for the interior of the gasifier (7). Examination of Table 2 reveals that there is sufficient CO , CO_2 , H_2 , H_2O , and H_2S to provide a sizeable amount of oxygen and sulfur via the equilibria

$$CO + 1/2\ O_2 \rightleftarrows CO_2 \ , \qquad (1\text{-}3)$$

$$H_2 + 1/2\ O_2 \rightleftarrows H_2O \ , \qquad (1\text{-}4)$$

Table 3. Composition of Illinois #6 ash and coal char (6).

ASH	Percentage
SiO_2	46.3
Al_2O_3	15.2
Fe_2O_3	14.9
CaO	6.5
MgO	1.1
TiO_2	0.6
P_2O_5	0.2
Na_2O	3.0
K_2O	1.8
SO_3	5.4
	as sulfate

CHAR	Percentage
carbon	25-50%
ash	45-70%
sulfur	<1.5%
high boiling tars	<4%

and

$$H_2 + 1/2\ S_2 \rightleftarrows H_2S \ . \qquad (1\text{-}5)$$

From these reactions and the temperatures at which these plants operate, it is apparent that the alloys can undergo extensive and rapid corrosion. This field is a popular and extensive one, and high-temperature corrosion of metals has been discussed by many authors (8-10). The corrosion reactions of interest here are oxidation and sulfidation:

$$xM + y/2\ O_2 \rightleftarrows M_xO_y \qquad (1\text{-}6)$$

and

$$xM + y/2\ S_2 \rightleftarrows M_xS_y \qquad (1\text{-}7)$$

where M represents a metal in the alloy. Oxidation is of interest because many iron-base alloys must be designed to resist the formation of iron oxide. This is usually done by the addition of chromium to the alloy, so that Cr_2O_3 forms on the alloy rather than any of the iron oxides. Cr_2O_3 is a stable, defect-free oxide that serves as an effective barrier to internal oxidation since the diffusivity of oxygen in it is quite low (11). Similarly, additions of Al to iron-base alloys results in the formation of Al_2O_3 layers and prevents internal oxidation.

High-temperature sulfidation is a different matter entirely. Whereas some oxides are dense and relatively defect-free and can serve as protective barriers (11), no sulfide is. Worse yet, in the temperature range of a gasifier (800-1000°C), some of the sulfide or sulfide-containing phases are liquid, in particular the Ni-NiS

eutectic (m. p. ≈ 650°C) and the FeO-FeS eutectic (m. p. ≈ 950°C). The problem of gas-phase corrosion then involves determining what phases can be formed in the conditions prevalent in a gasifier and whether these phases are protective or detrimental.

As has been previously indicated, there is a solid particulate phase present in a gasifier. This is coal char. As it flows through the internals of the gasifier, it is possible for the char to collect in pockets in tubes and bends. These particles are very small, ranging in size from less than 10 μm to as much as 250 μm. From Table 3 it is observed that char contains traces of fixed inorganic sulfur besides the usual carbon and ash. It is appropriate to ask if there is sufficient sulfur in the char to act as a corrosive agent at the temperature and oxygen and sulfur potentials of a gasifier. From coal analyses (12), it has been shown that considerable sulfur is present in coal as sulfates, sulfides, and organic sulfur. After processing, does sufficient sulfur remain in the char?

D. Preliminary Screening Experiments

In order to test the hypothesis that there is sufficient sulfur present in char to corrode iron-base alloys, several screening experiments were proposed and carried out (13). Three different alloys, Fe-10Al , Fe-10Al-5Cr , and Fe-10Al-10Cr , were exposed to char at 982°C. Argon containing 6 to 10 ppm O_2 was fed into the furnace, and the samples were exposed for periods of 24, 50, and 100 hours. After 24 and 50 hours, all three alloys exhibited similar behavior--formation of external Al_2O_3 layers with relatively little internal penetration (see Figure 3). The aluminum and chromium x-ray maps show that the oxidation of the

Figure 3. Cross sections of samples exposed to char and argon (containing 6 to 10 ppm O_2) for 24 hours at 982°C. The attached x-ray maps show elemental distributions as indicated. (a) Fe-10Al alloy. Note the heavy, thick protrusion. (b) Al x-ray map of protrusion indicates that protrusion is Al_2O_3. (c) Fe-10Al-5Cr alloy. Note the heavy, dark gray inclusion. (d) Al x-ray map indicates inclusions are Al_2O_3. (e) Fe-10Al-10Cr alloy with dark gray inclusions. (f) Cr-map showing Cr enrichment adjacent to but not in scale. (g) Al-map showing scale is Al_2O_3.

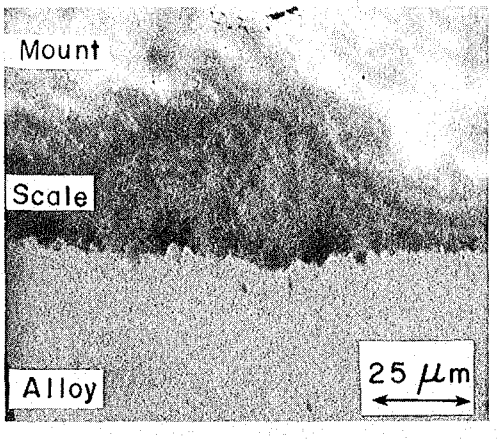

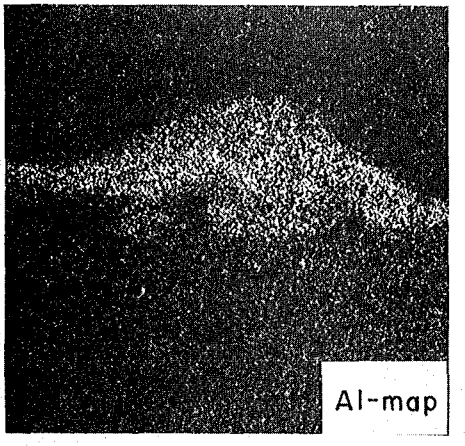

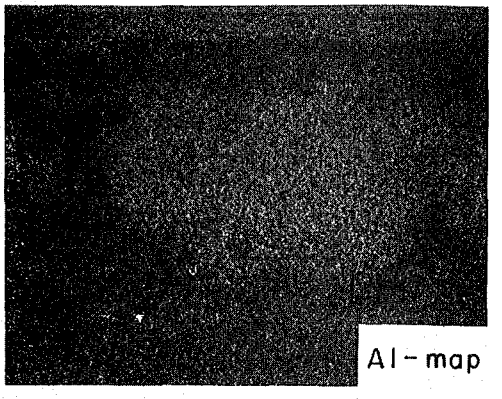

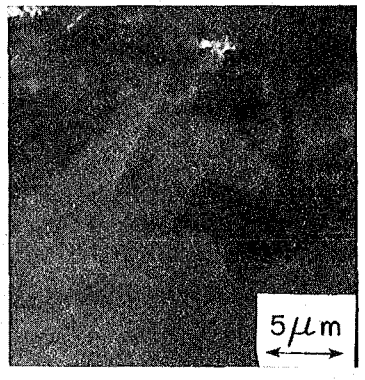

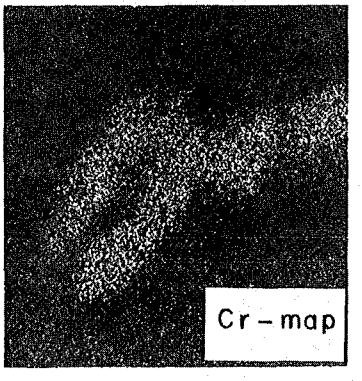

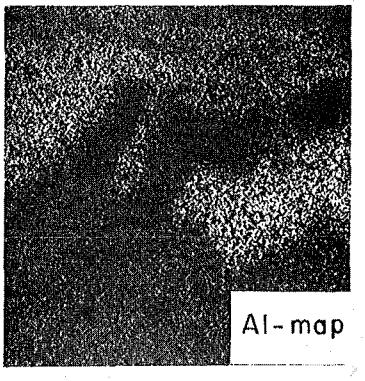

XBB 779-8963

alloy is confined to the surface, which is expected because of the high aluminum content of these alloys. After 100 hours, the situation has altered drastically in the case of the Fe-10Al and Fe-10Al-5Cr alloys. There is considerable internal penetration (see Figure 4) of the alloy. Although Al- and Cr-rich regions can be observed at the top of Figure 4a, indicating the presence of Al_2O_3 and Cr_2O_3 layers, x-ray mapping indicates the presence of Al-rich sulfides deep in the bulk of the alloy (Figure 4c,d). The sulfur can come from nowhere but the char. The reasons for this massive internal attack are discussed elesehwere (6), but the important result remains that there is sufficient sulfur in some form in char to attack these alloys.

E. Purpose of Research

In the screening experiments (see Section D), the oxygen potential was largely uncontrolled, being set only by the oxygen present in the argon and by the reaction

$$C + 1/2\ O_2 \rightleftarrows CO\ . \qquad (1\text{-}8)$$

As the carbon was oxidized and used up, the oxygen partial pressure could rise to that value present in the argon, about 10^{-5} to 10^{-6} atmospheres. Although from these experiments it is known that there is sufficient sulfur present to be corrosive, it is not known from these experiments what the precise conditions are at which that sulfur can attack the alloy.

The purpose of this research is to separate the effects of char and gas-composition on corrosion. It is desired to study only the effects that char has on iron-base alloys in the conditions of temperature and oxygen potential that prevail in the internals of a coal gasifier.

Figure 4. Cross section and x-ray mappings of Fe-10Al-5Cr alloy after 100 hours exposure to 982°C and argon combining 6 to 10 ppm oxygen. (a) Electron image. (b-e) elemental maps as indicated. Note the four distinct regions in the cross section: 1) lightest gray region is alloy itself, 2) medium gray at top of (a) is a chromium oxide (see e), 3) darker gray below that is aluminum oxide (see c and d), and 4) the dark gray inclusions in bulk of alloy are aluminum-rich sulfides (see c and d). Iron is excluded from the aluminum-containing regions (see b).

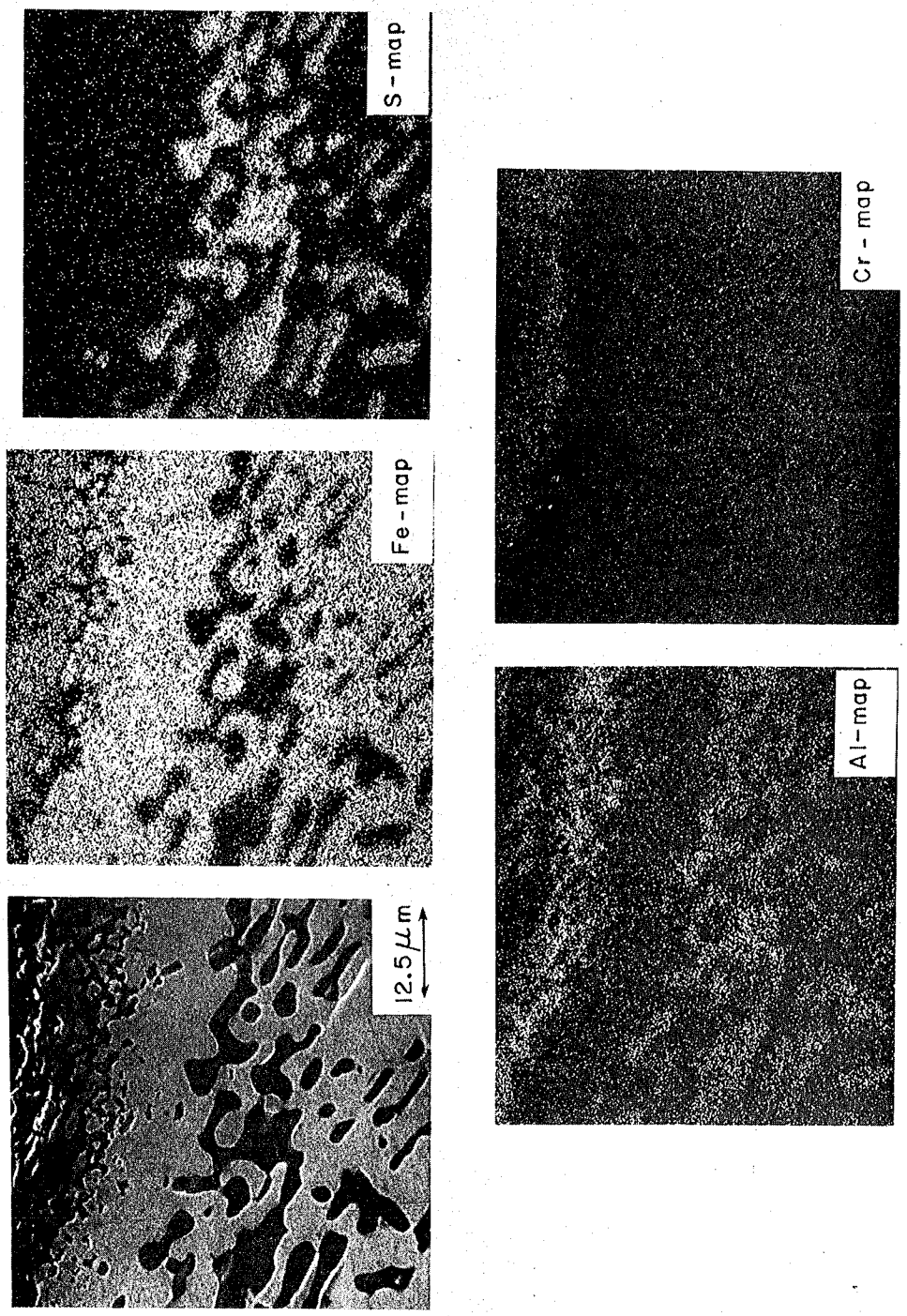

XBB 779-8965

CHAPTER 2

Thermodynamics

Any description of a set of possible chemical reactions relies on thermodynamics and kinetics to predict the reaction products. Thermodynamics determines which reactions in the set are most likely, and kinetics determines which will occur most rapidly. Of the two, kinetics is more important. It is often observed that when two reactions compete, the one that is formed most rapidly will predominate, even when thermodynamically the other is favored. But the kinetics of a reaction are difficult to predict even when a model for a mechanism is available, and when no model is available, it becomes almost entirely empirical. High temperature corrosion is particularly complicated. Not only is the gas phase multi-component, but so is the solid phase. Worse even than this, the solid phase is heterogeneous, and different regions of the alloy surface may have substantially different compositions. Since a kinetic/mechanistic explanation of alloy behavior is impossible given such complications, a thermodynamic explanation will have to serve with the understanding that thermodynamics explains only part of the story, albeit a very important one.

A. Gas-Phase Corrosion

When the topic of corrosion is discussed, a number of kinds of corrosion are possible: molten salt, aqueous, electrochemical, etc. Of all of these, the concern here will be specifically with gas-phase oxidation and sulfidation. As explained in Chapter 1, these two are the principal corrosion pathways in high temperature coal processing units.

Since all coal-burning power plants and processing units operate in regions where a number of metal oxides can be formed, oxidation is of particular interest. Most oxides form internally as well as on the surface of the alloy. This results from inward diffusion of oxygen along grain boundaries and surface defects and can occur with sufficient rapidity to shorten severely the lifetime of the alloy (14). If the lattice structure of the oxide is regular and free of interstitial atoms and vacancies, the formation of internal oxide inclusions can proceed with a relatively small change in volume within the alloy. This is usually not the case (15). Most oxides have a tremendously expanded and non-stoichiometric structure, and the formation of inclusions results in the region of the alloy surrounding the oxide inclusion undergoing severe growth stresses. If the inclusion is formed near the surface of the alloy, the growth-induced stresses may be sufficient to break up the structure of the surface. This process presents fresh alloy to the environment and hastens ultimate material failure.

Not all oxides have this effect on iron-base alloys. Some oxides, in particular Cr_2O_3 and Al_2O_3, not only grow rapidly but are very stable. Their lattice structures are dense, regular, and do not have the large concentrations of vacancies and defects which characterize non-stoichiometric oxides (16). Diffusion in these oxides proceeds by a lattice mechanism rather than by a defect mechanism. In solids, lattice diffusion coefficients are of the order of 10^{-12} - 10^{-14} m^2/s at 900°C whereas defect diffusion coefficients can be as large as 10^{-7} - 10^{-8} m^2/s at the same temperature (17). It then becomes apparent that diffusion through Cr_2O_3 and Al_2O_3 will be much slower than

through FeO , Fe_2O_3 , NiO , and other common oxides.

The formation of uniform Cr_2O_3 and Al_2O_3 layers begins to occur on the surface above certain bulk concentrations of Cr or Al . For Cr the level is about 18 to 20% (wt.) for Fe-base alloys (18) and for Al it is about 5% (wt.) (19). This is an important advantage. Once the oxide is formed, it creates a barrier to further inward diffusion of oxygen. These protective Al_2O_3 and Cr_2O_3 scales are responsible for the generally good corrosion resistance of high-Cr and high-Al content alloys.

Sulfides provide no such protection. All have very defective, non-stoichiometric structures, and all grow fairly rapidly. A protective oxide barrier can slow down the process, but eventually sufficient sulfur can get through the surface scale to attack the alloy. Figure 5 shows a possible mechanism for the internal sulfidation of an alloy through a protective scale. Once the rapidly-growing oxide scale is formed (Figure 5a), inward diffusion of sulfur is considerably hindered. But sulfur diffusion by the lattice or volume mechanism or down oxide grain boundaries can still occur (Figure 5b). Eventually as Figure 5c shows, just beneath the oxide layer a sulfide inclusion can form. Since the lattice structure of the sulfide is very defective, the formation of the inclusion results in a very large increase in local volume. In Figure 5d, this fractures the oxide scale and presents fresh alloy for attack. The formation of the Cr_2O_3 or Al_2O_3 layer results in the depletion of Cr or Al from the alloy at the oxide/alloy interface. There may be insufficient Al or Cr to reform an oxide scale as a result, leaving the alloy particularly vulnerable to internal attack.

Figure 5 (a). Formation of a compact oxide side in an environment containing both oxygen and sulfur. The surface oxidizes more rapidly than it sulfidizes.

Figure 5 (b). Diffusion of sulfur down grain boundaries. At the alloy/scale interface, there is insufficient oxygen to continue the formation of an oxide scale.

Figure 5 (c). After a sufficient period has passed, sulfide inclusions can form at alloy/scale interface.

Figure 5 (d). These inclusions can become large enough to fracture the oxide scale and severely disrupt the integrity of the protective barrier.

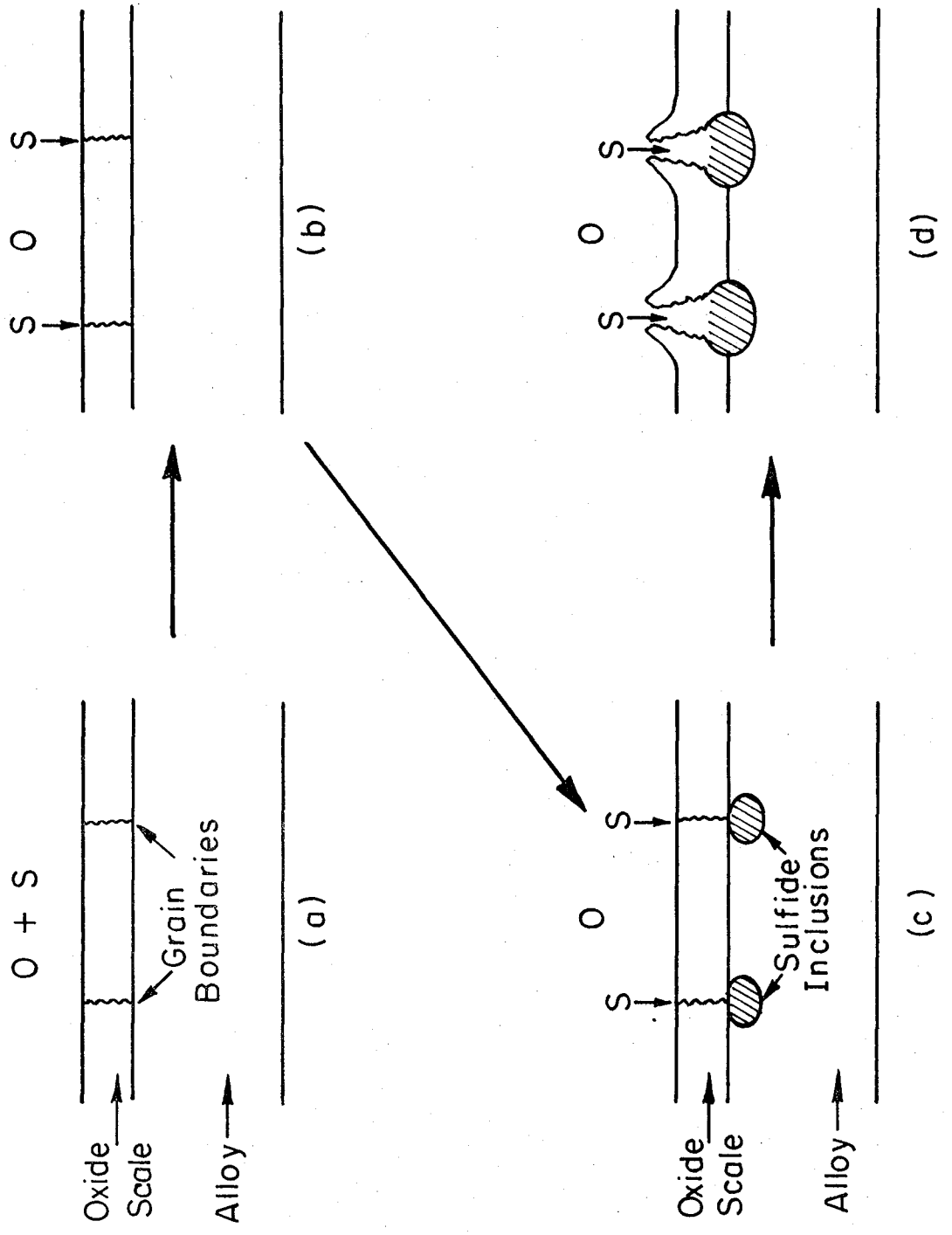
O + S
Grain Boundaries
Oxide Scale
Alloy
(a)
S
O
S
(b)
S
O
S
Sulfide Inclusions
(c)
S
O
S
(d)

XBL 781-4507

There is an additional problem that arises as a consequence of sulfidation of iron-base alloys: some sulfides are liquid. Table 4 shows the typical sulfides that can be commonly found on iron-base alloys and their melting points. Most melt in the 1100-1300°C range, well above 1000°C. But the nickel sulfides, NiS and Ni_3S_2, melt at less than 800°C. This is of particular concern in the Fe-Cr-Ni ternary (300 series stainless steels) which has sufficient Ni to provide considerable high temperature strength. If a liquid sulfide can form underneath a protective Cr_2O_3 scale, it can conceivably float the scale off on a layer of liquid, ruining the protection that the alloy obtained from the Cr_2O_3 scale. Even if Ni is eliminated entirely from the alloy system, as in the Fe-Cr-Al system, the problem of liquid layer formation is not eliminated. The FeO-FeS eutectic melts at about 950°C. This is a more difficult problem to deal with. Iron cannot be eliminated as a practical base for economical high-temperature alloys.

If, as it appears, it is impossible to develop a sulfidation resistant iron-base alloy, the next best approach is to be able to predict the sulfides and oxides that will be formed under specific conditions. This can be approximated by using a thermodynamic approach.

B. Equilibrium Thermodynamics of Gas-Phase Corrosion

For a general chemical reaction of the form

$$aA + bB \rightleftarrows cC + dD \qquad (2\text{-}1)$$

there is associated a Gibbs energy ΔG_r^o such that (20)

$$\Delta G_r^o = -RT\ln K_{eq} \qquad (2\text{-}2)$$

Table 4. Melting points of sulfides important in iron-base alloys containing Al , Cr , and/or Ni .

Compound	M. P. (°C)
FeS	1195
FeS_2	1171
Al_2S_3	1100
CrS	1550
Cr_2S_3	1350
NiS	797
Ni_3S_2	790

where K_{eq} is the equilibrium constant and is defined by the equation

$$K_{eq} = \frac{(a_C)^c (a_D)^d}{(a_A)^a (a_B)^b} \qquad (2\text{-}3)$$

where the a's are the activities of the various species.

Consider a general oxidation reaction occurring between a gas phase and an alloy. In this case, eq. (2-1) becomes

$$xM + y/2\ O_2 \rightleftarrows M_xO_y \ . \qquad (2\text{-}4)$$

The following result is obtained from equations (2-2) and (2-3):

$$\Delta G_r^o = -RT\ln \frac{\left(a_{M_xO_y}\right)}{(a_M)^x \left(a_{O_2}\right)^{y/2}} \qquad (2\text{-}5)$$

In order to describe this system completely, it is necessary to have information on the activities of the various species at the reaction conditions. This information is usually not available, but it is possible to make some reasonable assumptions.

The vapor phase can be assumed to be ideal since the total pressure is low and the temperature is high in these experiments. Therefore, for a first approximation the oxygen activity is assumed to equal the oxygen partial pressure, P_{O_2} .

Some information on the activities of the solid phases (alloy and scale) is required. Some is available for specific systems (21,22), but in general there is no way to predict the activity of a metal in an alloy. Even when data are available, assumptions have to be made to justify their use in equation (2-5). If the activity a_M is defined by

$$a_m = \gamma_M x_M \qquad (2\text{-}6)$$

where γ_M is the activity coefficient and x_M is the mole fraction of M in the alloy, then it is necessary to determine γ_M.

Such data are not complete and, when available for ternary alloy systems, are often calculated from binary systems. For a first approximation, it is often sufficient to treat the solid solution as ideal and the activity is taken to be equal either to the mole fraction of the metal in the alloy, or to 1. As will be shown in the next section, this does not invalidate the use of thermodynamics in predicting gas-phase corrosion.

C. Thermodynamic Stability Diagrams

If the metal and the oxide are insoluble in each other and the fugacity of the oxygen is equal to its partial pressure, P_{O_2}, then equation (2-5) can be rearranged to give

$$P_{O_2} = \left[\exp\left(\frac{\Delta G^o_r}{RT}\right)\right]^{2/y} . \qquad (2\text{-}7)$$

The dissociation pressure for a given oxide can then be determined from the Gibbs energy and temperature of the reaction. At a partial pressure of oxygen greater than that determined by equation (2-7) the oxide will be stable, and at a lower P_{O_2} the oxide will be unstable. Similar calculations can be performed using Gibbs energy data for the formation of sulfides and replacing P_{O_2} by P_{S_2}.

These calculations can be combined in a two-dimensional isotherm that plots the stable phases as a function of oxygen and sulfur partial

pressures. Such a plot is called a thermodynamic stability diagram. These diagrams have been used by a number of investigators as predictive devices for high-temperature corrosion in aggressive environments (25-27). Given reliable and consistent thermodynamic data for the formation of the oxides and sulfides, stability diagrams are easy to construct for pure metals. For alloys, the situation is more complicated. Bimetallic oxides (spinels) may be formed as a result of interaction between phases. For the Fe-Cr-Al system:

$$Fe + 1/2\ O_2 + Cr_2O_3 \rightleftarrows FeCr_2O_4 \qquad (2\text{-}8)$$

$$Fe + 1/2\ O_2 + Al_2O_3 \rightleftarrows FeAl_2O_4 \qquad (2\text{-}9)$$

$$FeO + Cr_2O_3 \rightleftarrows FeCr_2O_4 \qquad (2\text{-}10)$$

$$FeO + Al_2O_3 \rightleftarrows FeAl_2O_4 \qquad (2\text{-}11)$$

$$FeS + Cr_2O_3 + 1/2\ O_2 \rightleftarrows FeCr_2O_4 \qquad (2\text{-}12)$$

$$FeS + Al_2O_3 + 1/2\ O_2 \rightleftarrows FeAl_2O_4 \qquad (2\text{-}13)$$

Since the data for the spinels are available but not complete, such interactions are often ignored in the prediction of alloy behavior from the stability diagrams.

Figure 6 shows the result of the above procedure (27). It represents the Fe-Cr-Al system at 982°C (1800°F). Since the vertical axis represents P_{S_2} and the horizontal axis P_{O_2}, horizontal lines represent metal-sulfide or sulfide-sulfide equilibria and vertical lines metal-oxide or oxide-oxide equilibria. Lines with a slope between zero and infinity represent equilibria between phases containing oxygen and/or sulfur. The arrows on the diagram indicate the line at which the particular phase becomes stable, and where the arrows overlap,

Figure 6. Thermodynamic stability diagram for the Fe-Cr-Al system represented at 982°C (1800°F). The arrows indicate P_{O_2} and P_{S_2} lines at which the specific oxide or sulfide phase becomes stable. The rectangular region indicates P_{O_2} and P_{S_2} ranges of typical coal gasifiers.

Key: —— ---- —— phase boundaries involving only Fe

---------- phase boundaries involving Al

———————— phase boundaries involving Cr

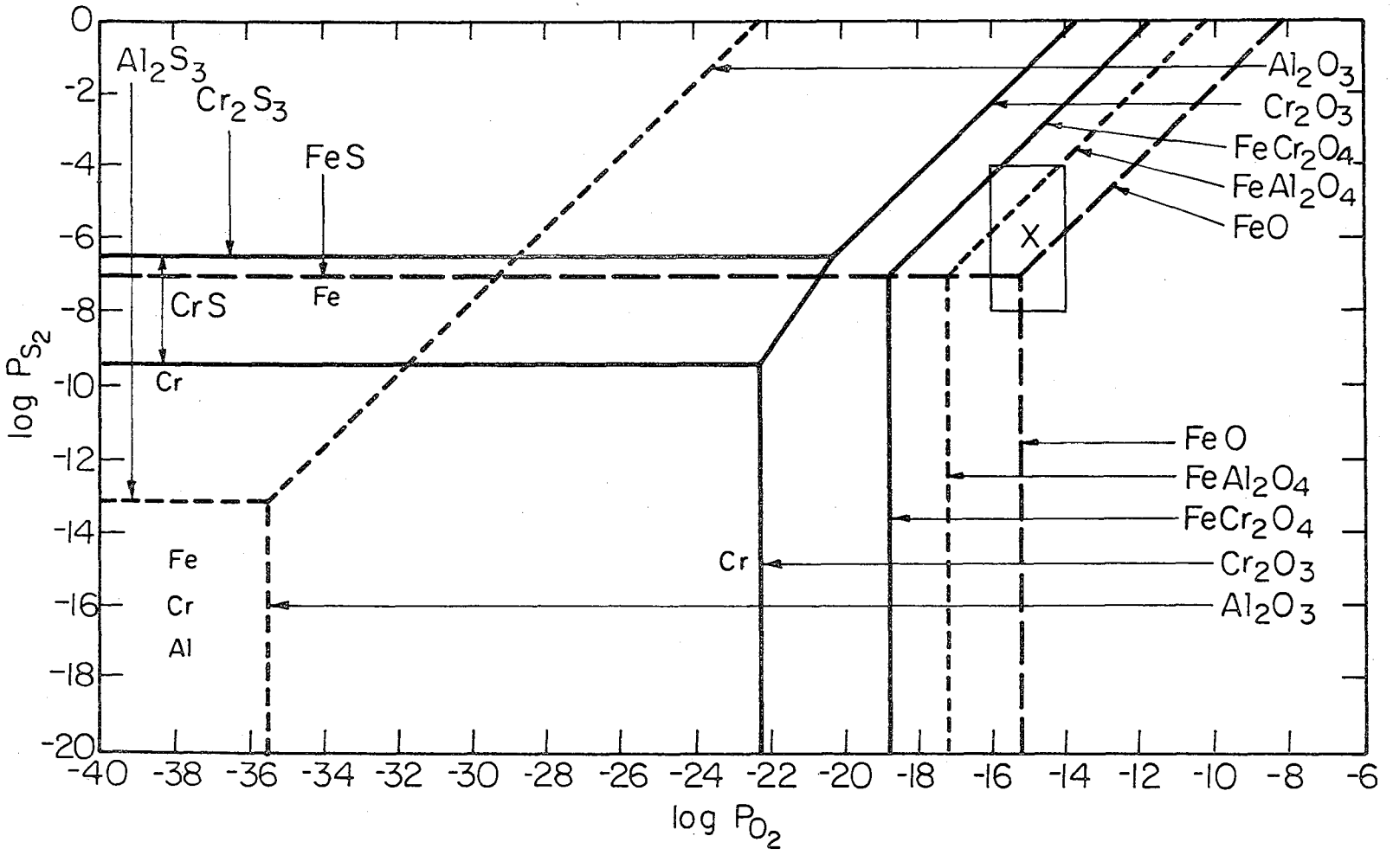

XBL781-4401

the phase stabilities overlap. Oxides of iron higher than FeO have not been considered on this diagram.

It appears on the diagram that at high P_{O_2}'s five phases can coexist: FeO , Al_2O_3 , $FeCr_2O_4$, Cr_2O_3 , and $FeAl_2O_4$. From stoichiometric considerations, some of these phases may not be possible since the spinels ($FeCr_2O_4$ and $FeAl_2O_4$) are combinations of the other three phases. Figure 7 illustrates that a maximum of three phases can co-exist in a given region on the diagram. If there is a stoichiometric excess of FeO (or FeS) , then Figure 7a shows that only FeO (FeS) , $FeAl_2O_4$, and $FeCr_2O_4$, will coexist. If there is insufficient iron, then the phases may be Al_2O_3 , $FeAl_2O_4$, and $FeCr_2O_4$. Figure 7b will apply as P_{O_2} decreases into a region where $FeAl_2O_4$ is not stable. Here Fe and Cr_2O_3 cannot coexist, and which is present depends on whether there is an excess of Fe or Cr . If there is insufficient oxygen to form either $FeCr_2O_4$ or $FeAl_2O_4$, then Figure 7c applies. This is merely a non-interacting mixture of the stable forms of the three metals.

Similar constructions can be made for the Fe-Cr-Ni system. Figures 8 and 9 present the stability and stoichiometric diagrams at 982°C for this ternary system.

The rectangular region in the diagram represents P_{O_2} and P_{S_2} ranges for typical gasifier gas compositions (Table 2). The "x" mark in the middle of the rectangle indicates the experimental gas composition at which the stable phases predicted in the diagrams were correlated with experiment (27). From Figures 6 and 7, the predicted phases are $FeAl_2O_4$, $FeCr_2O_4$, and Al_2O_3 if it is assumed there is sufficient Al to form an Al_2O_3 layer. Representative samples from

Figure 7 (a). Triangular diagram showing how the stoichiometry determines which phases are actually present when the stability diagram indicates that five phases are possible. The scales are intended to represent atomic percent of the metals on an oxygen- and sulfur-free basis. A point within a region on the diagram indicates a mixture of the three phases at the corners of the region. A point on a line indicates a mixture of the two phases at the ends of the line. As drawn, this figure applies to the right side of the stability diagram. It could represent the other two regions where five phases are possible if FeO is replaced by either Fe or FeS .

Figure 7 (b). Triangular diagram showing how the stoichiometry determines which phases are actually present when the stability diagram indicates that four phases are possible. As drawn, this figure applies to the bottom of the stability diagram in a region where $FeAl_2O_4$ is no longer stable.

For a similar region toward the top of the stability diagram, this figure applies with Fe replaced by FeS .

Figure 7 (c). Triangular diagram showing how the stoichiometry determines which phases are actually present when the stability diagram indicates that three phases are possible. As drawn, this figure applies to the bottom of the diagram in a region where $FeCr_2O_4$ is no longer stable.

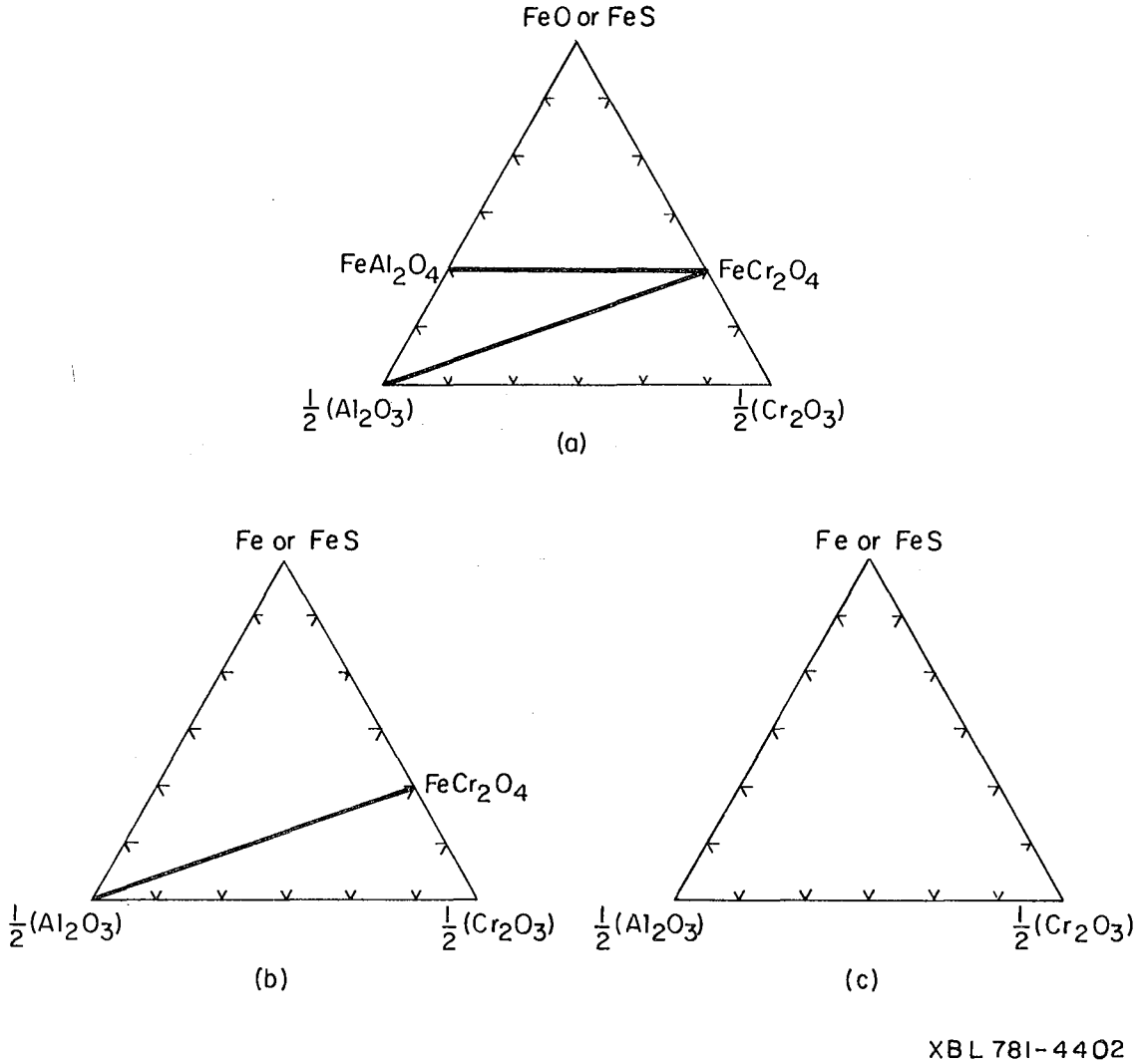
FeO or FeS
$FeAl_2O_4$
$FeCr_2O_4$
$\frac{1}{2}(Al_2O_3)$
$\frac{1}{2}(Cr_2O_3)$
(a)
Fe or FeS
$FeCr_2O_4$
$\frac{1}{2}(Al_2O_3)$
$\frac{1}{2}(Cr_2O_3)$
(b)
Fe or FeS
$\frac{1}{2}(Al_2O_3)$
$\frac{1}{2}(Cr_2O_3)$
(c)

XBL 781-4402

Figure 8. Thermodynamic stability diagram for the Fe-Cr-Ni system represented at 982°C (1800°F). The arrows indicate P_{O_2} and P_{S_2} lines at which the specific oxide or sulfide phase becomes stable. The rectangular region indicates P_{O_2} and P_{S_2} ranges of typical coal gasifiers.

Key: —— —— —— phase boundaries involving Fe

---------- phase boundaries involving Ni

———————— phase boundaries involving only Cr

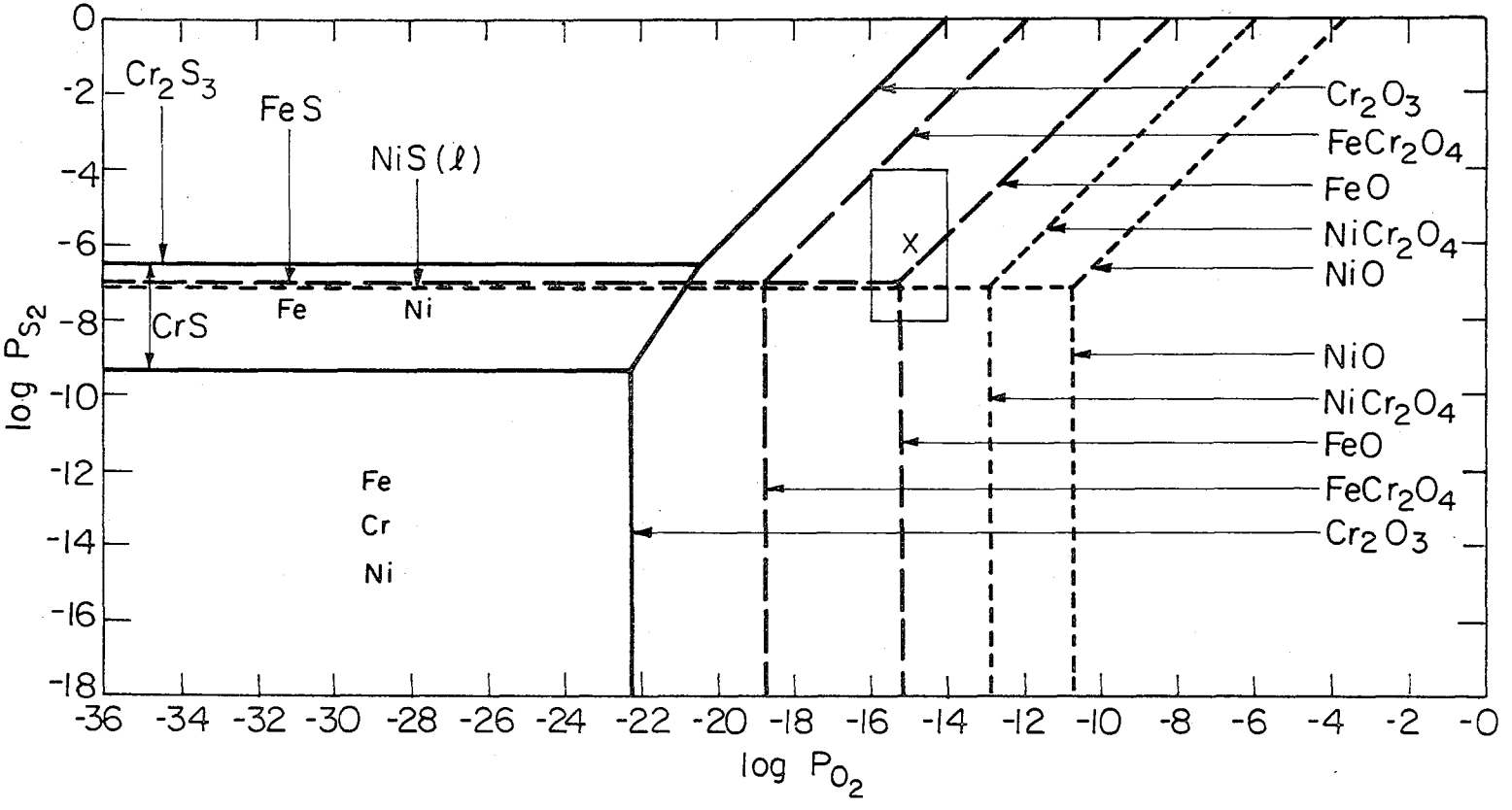
0
-2
-4
-6
-8
-10
-12
-14
-16
-18
log P_{S_2}
Cr_2S_3
FeS
NiS (ℓ)
CrS
Fe
Ni
X
Fe
Cr
Ni
Cr_2O_3
$FeCr_2O_4$
FeO
$NiCr_2O_4$
NiO
NiO
$NiCr_2O_4$
FeO
$FeCr_2O_4$
Cr_2O_3
-36 -34 -32 -30 -28 -26 -24 -22 -20 -18 -16 -14 -12 -10 -8 -6 -4 -2 -0
log P_{O_2}

XBL 781-4447

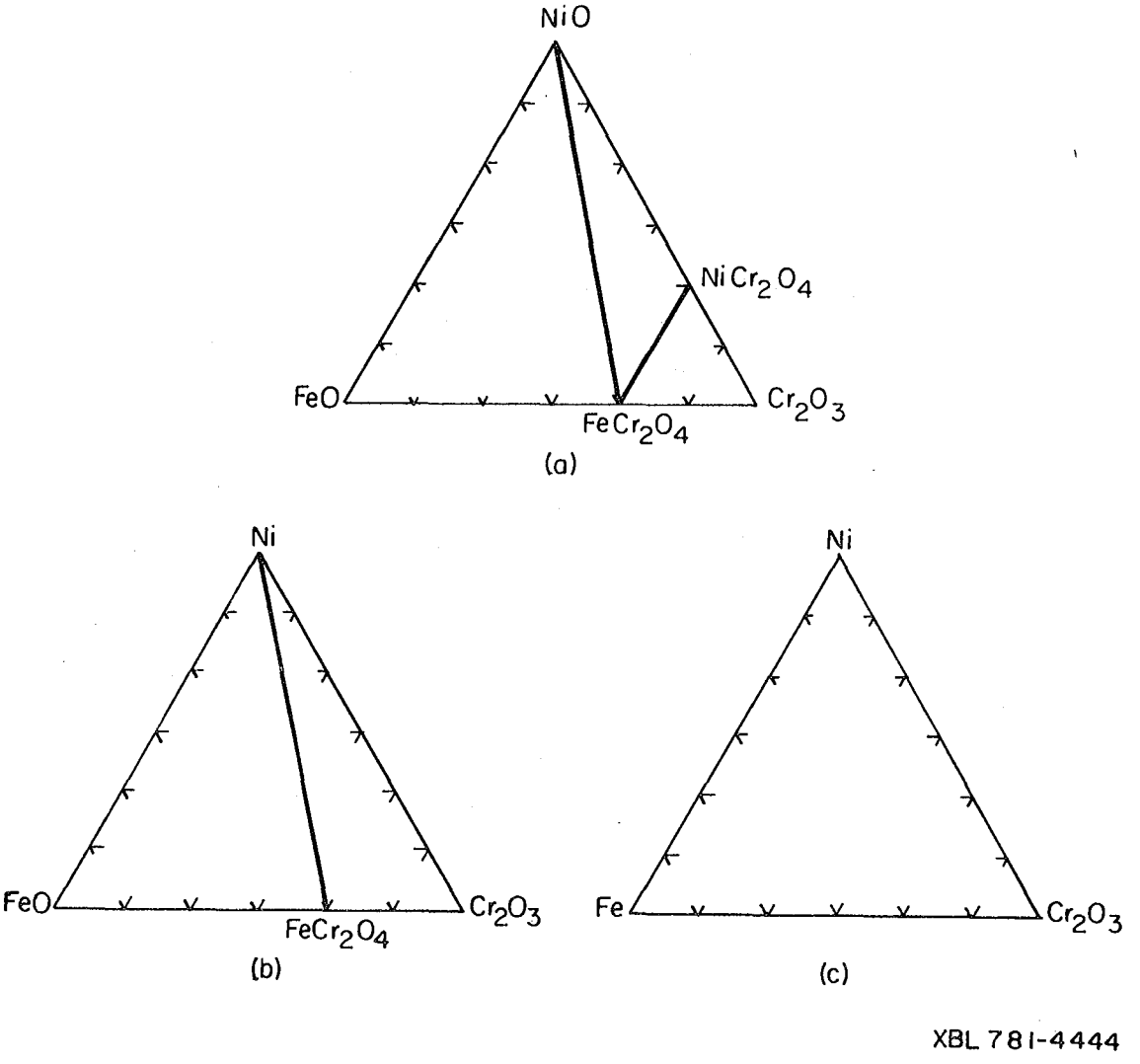

Figure 9. Triangular diagrams showing how the stoichiometry determines which phases are actually present when the stability diagram indicates that 3 or more are possible.

a) Applies in a region where five phases are possible, i.e. the right side of the Fe-Cr-Ni diagram. It could represent the other two regions where five phases are possible if NiO is replaced by either Ni or NiS(ℓ) .

b) Applies in a region where four phases are possible. As drawn, this figure applies to the bottom of the stability diagram in a region where $NiCr_2O_4$ is no longer stable. For a similar region toward the top of the diagram, this figure applies with Ni replaced by NiS(ℓ) .

c) Applies in a region where three phases are possible. As drawn, this figure applies to the bottom of the diagram in a region where $FeCr_2O_4$ is no longer stable.

the Fe-Cr-Al system were exposed for 48 hours (see Table 5 for compositions). Only on the Fe-10Al binary was any $FeAl_2O_4$ observed. All others showed only the presence of Al_2O_3 scales. However, powder mixtures of FeS/Al_2O_3 and FeS/Cr_2O_3 showed the presence of both spinels as predicted by the diagrams. There may be severe kinetic limitations on the formation of the spinels, or FeS , which is unstable at the experimental conditions, may be a necessary precursor to the formation of the spinels via reactions (2-12) and (2-13).

Thermodynamic stability diagrams have a definite use as predictive devices for high-temperature gas-phase corrosion as long as their limitations are understood. For corrosion by coal char, they are not nearly so useful. Conditions at the char/alloy interface may be significantly different from those in the gas phase.

Table 5. Alloys used in comparison of predicted phases with observed phases.

(1)	Fe-10Al
(2)	Fe-10Al-5Cr
(3)	Fe-10Al-10Cr
(4)	Fe-10Al-15Cr
(5)	Fe-18Cr-5Al
(6)	Fe-18Cr-7Al

CHAPTER 3

Experimental and Results

A. Equipment

The furnace used was a vertical tube-type furnace designed to isolate the specimens from each other. Figure 10 shows the complete furnace. It is a triple tube furnace using wound and potted Kanthal tube heaters. They maintained the temperature to within ± 2°C of the setpoint. The tubes are high purity quartz glass fitted with standard-taper fittings and held together with springs. Figure 11 shows the furnace with two tubes withdrawn from the furnace and one disassembled to remove the sample. The samples are held in a quartz cup and covered with char or char substitute and placed in the sample tubes (see Figure 11). The sample tubes are then hung by springs from the top portion of the furnace.

All the specimens, about 1 cm x 1 cm x 0.1 cm, were ground to 600 grit with silicon carbide paper and cleaned with alcohol and acetone. They were placed in the sample tubes, which were then assembled onto the furnace. The tubes were first flushed with argon for ten minutes to remove all traces of atmospheric oxygen and then flushed with either CO or CO/CO_2 to remove the argon. The sample tubes were inserted into the furnace, and the temperature adjusted, which requires about ten minutes. After the desired exposure time, the sample tubes were pulled out of the furnace heat zone, flushed with argon, and allowed to drop to a suitably low temperature for handling. This requires less than ten minutes due to the low mass of the furnace tubes. The samples were then removed for analysis.

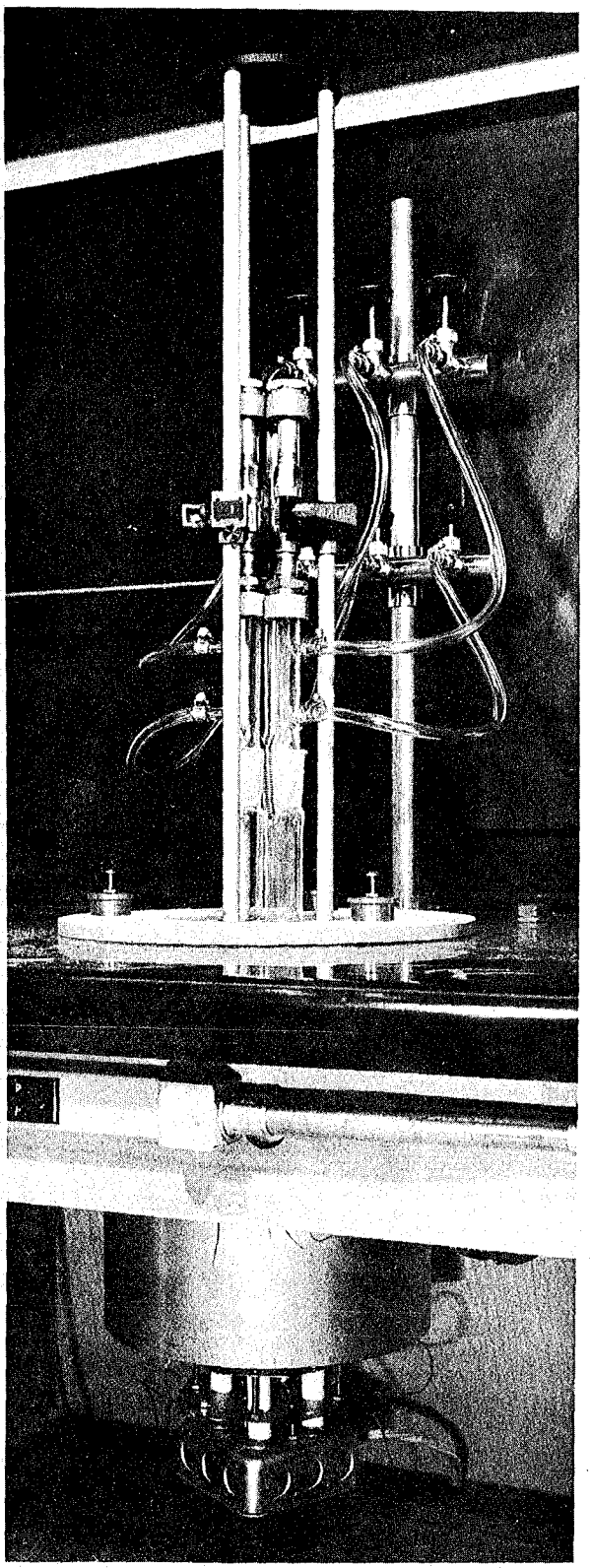

XBB 781-776

Figure 10. Overall picture of furnace with sample tubes inserted into heat zone.

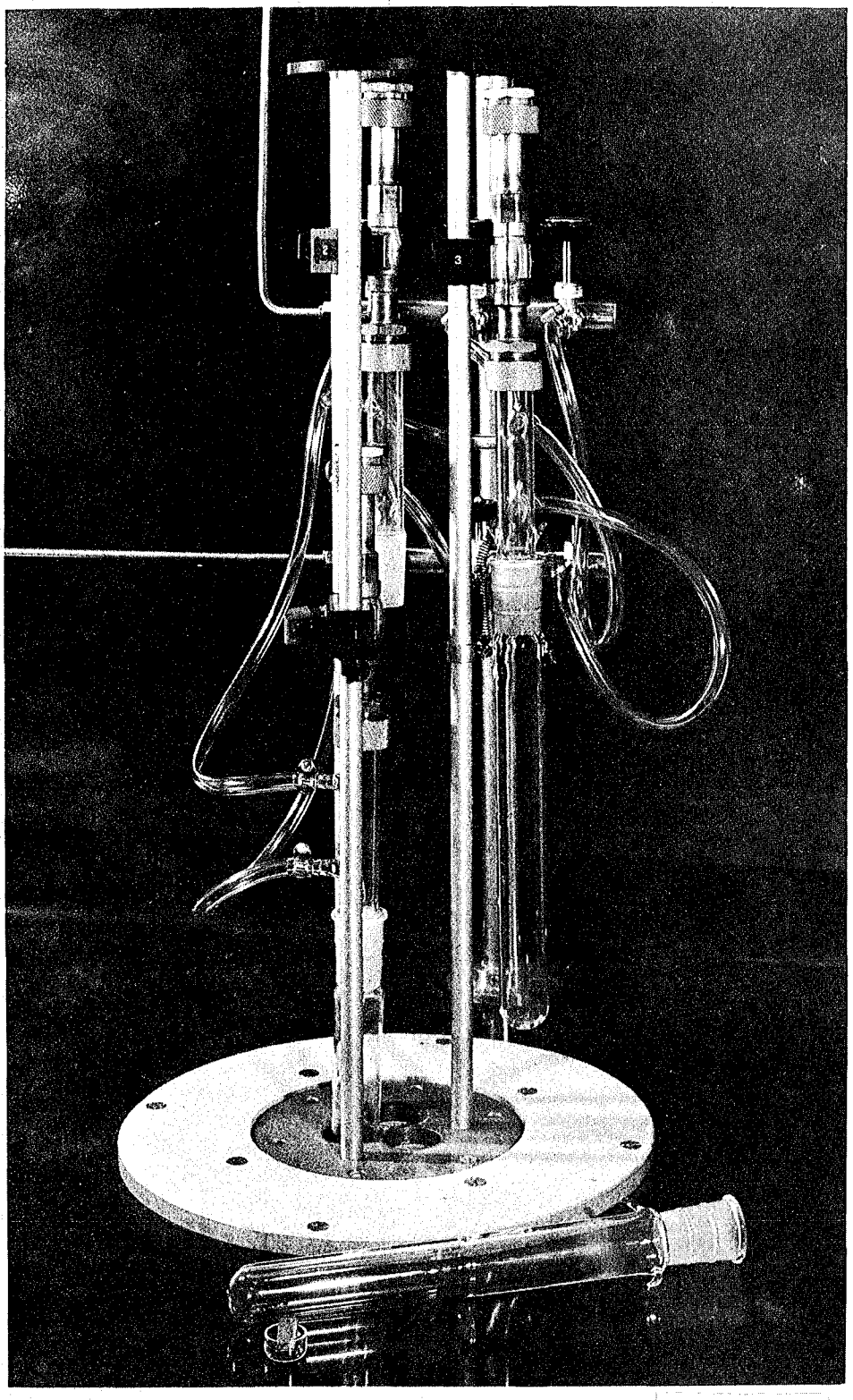

XBB 781-777

Figure 11. Furnace tubes showing arrangement of samples.

A constant P_{O_2} in the gas mixture was maintained using either pure CO gas or pre-mixed CO/CO_2 containing 38.42% CO and 61.58% CO_2. The P_{O_2} was determined using either reactions (1-3) or (1-8). To insure a sufficient residence time for equilibration, the gas flow rate was kept to less than 20 cm^3/min. Uniform mixing was maintained by natural convection resulting from half the tube being held in the heat zone and half at room temperature (see Figure 12). Table 6 shows P_{O_2}'s determined by either the C/CO or the CO/CO_2 equilibrium at both temperatures. These are calculated results based on Gibbs energy data available in the JANAF tables (28) and are not measured values.

Following exposure, the samples were examined by scanning electron microscopy (SEM) for surface corrosion morphology. They were then mounted in a mixture of bakelite and phenolic plastic, ("Klarmount," supplied by Klarnell Corp.) especially designed for retention of scale and edges. The samples were cross-sectioned by grinding through the surface with 320 grit silicon carbide paper and then smoothing with 600 grit silicon carbide paper. They were next mounted in a rotary polishing unit (LECO Corp.) and polished for 2-6 hours on a nylon cloth with cerium oxide paste thinned with distilled water. The final polish was done with cerium oxide on microcloth for ten minutes. This technique insured maximum retention of edges plus a uniformly polished flat surface.

B. Synthetic Char

The purpose of this research is to isolate the attack of the alloys by coal char from the attack by a reactive gas. It is therefore necessary to isolate those species in the char which are responsible

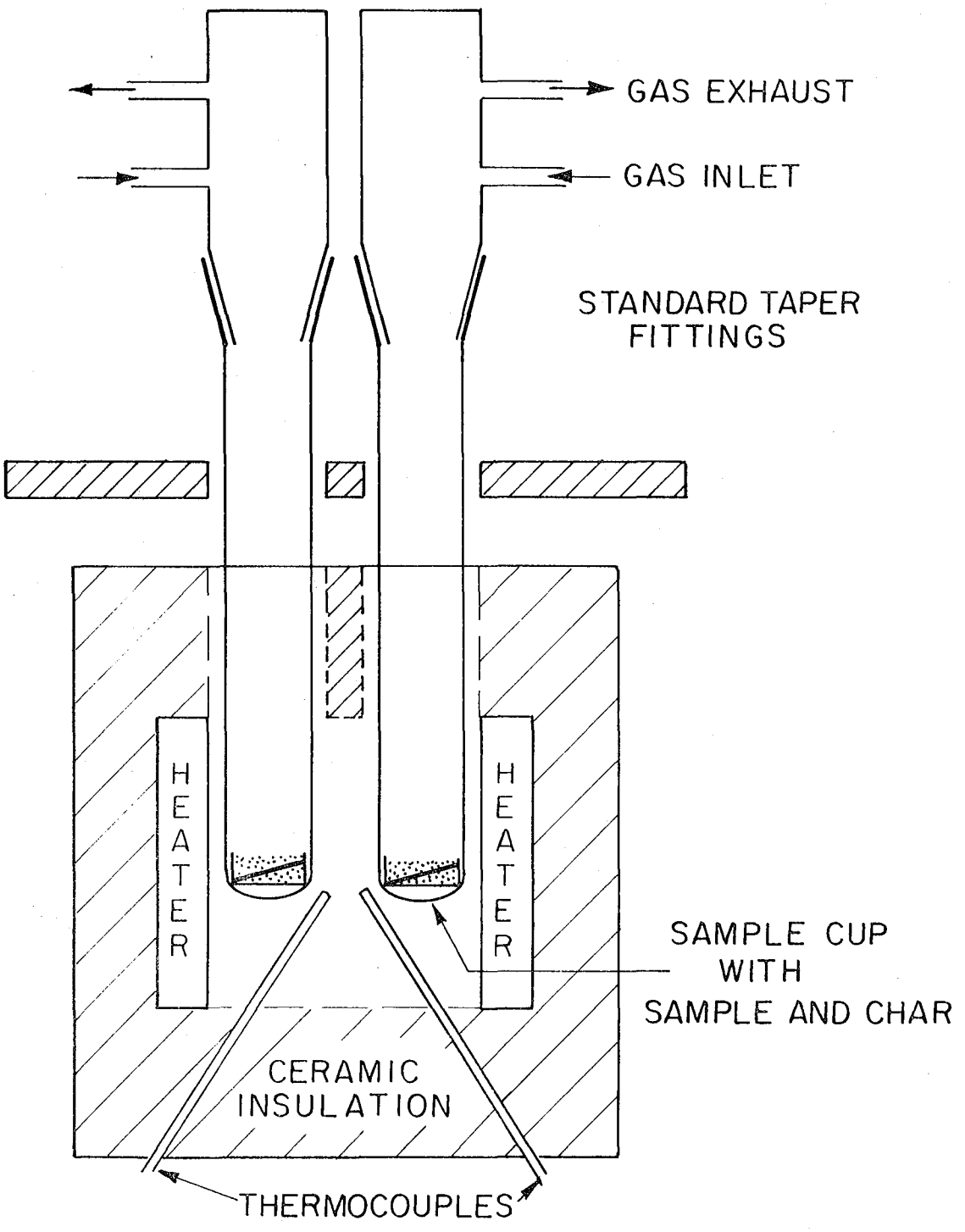

Figure 12. Cross-section of furnace.

Table 6. P_{O_2}'s determined by either C/CO or CO/CO_2 equilibria at the indicated temperatures (in atmospheres).

	871°C	982°C
C/CO	4.0×10^{-20}	1.0×10^{-19}
CO/CO_2	4.8×10^{-17}	4.2×10^{-15}

for the attack. It has already been mentioned that coal and coal char both contain inorganic sulfides and sulfates (12) in sufficient amounts to cause sulfidation of iron-base alloys (6). Next it is necessary to determine the principal species present in the char that is responsible for the observed corrosion.

To this end, several synthetic mixtures were made. It is postulated that the probable species responsible for the corrosive sulfur attack is either FeS or $CaSO_4$. Both of these are present in coal char, but it is uncertain which is responsible for the observed corrosion. Therefore, the synthetic chars contained either $CaSO_4$ or FeS in an amount typical of a char from a high sulfur coal - about 5 mole % sulfur. A neutral filler, Al_2O_3, was used to make up the bulk for those samples to be tested at $P_{O_2} = 10^{-15}$ to 10^{-17} atmosphere (CO/CO_2 equilibrium). For those samples to be run at $P_{O_2} = 10^{-19}$ to 10^{-20} (C/CO equilibrium), high purity graphite plus Al_2O_3 were used as fillers. The synthetic char mixtures used and the calculated P_{O_2}'s are shown in Table 7. Although these mixtures are designed to simulate the behavior of only one component present in coal char and not the behavior of char itself, those mixtures containing FeS will be called FeS-char and those containing $CaSO_4$ will be called $CaSO_4$-char.

The alloys used in these experiments were Fe-10Al, Fe-10Al-15Cr, commercial 310 stainless steel (Fe-25Cr-20Ni), and pure 310 stainless steel (no Si or Mn). It has already been observed that the binary corrodes relatively rapidly even though it has sufficient Al to form an Al_2O_3 layer (6). The addition of Cr appears to stabilize the Al_2O_3 layer and increase the corrosion resistance (6,27). The

Table 7. Char and synthetic char mixtures and the calculated oxygen partial pressures (in atmospheres).

Char mixture/gas phase	P_{O_2} 871°C	P_{O_2} 982°C
coal char/CO	4.0×10^{-20}	1.0×10^{-19}
FeS + Al_2O_3/CO/CO_2	4.8×10^{-17}	4.2×10^{-15}
$CaSO_4$ + Al_2O_3/CO/CO_2	4.8×10^{-17}	4.2×10^{-15}
FeS + Al_2O_3 + graphite/CO	4.0×10^{-20}	1.0×10^{-19}
$CaSO_4$ + Al_2O_3 + graphite/CO	4.0×10^{-20}	1.0×10^{-19}

addition of 15 wt% Cr is just less than that required for the formation of a Cr_2O_3 layer (18). These two alloys will test 1) rapid corrosion of the alloy and 2) stabilization of the Al_2O_3 layer. The other two alloys are Cr_2O_3 layer formers and represent a commonly used alloy system (Fe-Cr-Ni) for use in corrosive environments. They permit a comparison with the Fe-Cr-Al system in high temperature corrosion.

C. Experiments

Table 8 shows the experimental condition at which each test was run. The two 310 S.S. samples were placed in one tube such that they were not touching. The temperatures, 871°C and 982°C, were chosen to represent mean and maximum anticipated operating temperatures for coal gasifiers.

An additional short-term run was performed. This consisted of three separate Fe-10Al samples, each in Al_2O_3 + FeS in the CO/CO_2 mixture. They were held at 982°C for 1 hour, 2 hours, and 5 hours to observe the short term corrosion behavior of the alloy.

The oxygen potentials, ranging from 10^{-15} to 10^{-19} atmospheres at 982°C and from 10^{-17} to 10^{-20} atmospheres at 871°C, represent high and low values for P_{O_2} typical of coal gasifiers. These have an additional effect of providing a comparison of sulfidation by $CaSO_4$ and by FeS . $CaSO_4$ can provide sulfur for attack by reduction of the sulfate:

$$CaSO_4 \rightleftarrows CaO + 1/2\ S_2 + 3/2\ O_2 \ . \qquad (3\text{-}1)$$

Table 8. Experiments run using both coal char and synthetic substitution. Carbon is present as high purity graphite.

Char or Substitute	Gas Phase	Temperature (°C)	Exposure Time (hours)
coal char	CO	982	100
coal char	CO	982	50
coal char	CO	871	100
coal char	CO	871	50
5.91 mole % FeS + Al_2O_3	CO/CO_2	982	50
pure Al_2O_3	CO/CO_2	982	50
4.07 mole % $CaSO_4$ + Al_2O_3	CO/CO_2	982	50
5.91 mole % FeS + Al_2O_3	CO/CO_2	982	1, 2, 5
5.91 mole % FeS + Al_2O_3	CO/CO_2	871	50
4.07 mole % $CaSO_4$ + Al_2O_3	CO/CO_2	871	50
5.09 mole % FeS + Al_2O_3 + C	CO	982	50
5.00 mole % FeS + Al_2O_3 + C	CO	871	50
5.02 mole % $CaSO_4$ + Al_2O_3 + C	CO	982	50
5.02 mole % $CaSO_4$ + Al_2O_3 + C	CO	871	50

As the P_{O_2} decreases, the activity of the sulfur should increase. FeS can provide sulfur for internal attack by oxidation of the sulfide:

$$FeS + 1/2\ O_2 \rightleftarrows FeO + 1/2\ S_2 \ . \qquad (3\text{-}2)$$

As the P_{O_2} increases, the activity of the sulfur should increase. The important consideration here is the comparison of morphologies of corrosion by $CaSO_4$ and FeS and how these in turn compare with the morphology of corrosion by coal char.

D. Results

After 100 hours exposure in char and CO atmosphere at 982°C, considerable penetration into the alloy was observed on the Fe-10Al alloy. Figure 13a shows an optical cross-section of the alloy. Although there was no external growth of scale, the penetration looks like that in Figure 14, optical cross-sections of Fe-10Al and Fe-10Al-5Cr in char, argon, and 6 to 10 ppm O_2 (6). Note in particular (Figure 13a) the long, thin needles pointing in toward the bulk of the alloy. Another portion of the same cross-section is shown in Figure 13b along with energy dispersive x-ray analyses (EDAX) of the outer, middle, and inner portions of the penetrated region. The outer region as indicated by 13c appears to be a mixture of iron oxide and aluminum oxide. A more detailed analysis would have to be done to determine whether these were present as discrete compounds or as an iron-alumina spinel, i.e. $FeAl_2O_4$. Moving further in, 13d represents the large black inclusions. These appear to be entirely Al_2O_3 . At the inner edge of the penetration, a few of the elongated inclusions appear. These are analyzed in Figure 13e and contain a relatively large amount

Figure 13. Cross section of Fe-10Al alloy exposed to coal char for 100 hours at 982°C in pure CO .

a) Optical micrograph

b) Scanning electron photomicrograph

c) EDAX analysis of outer region of inclusions: Fe and Al-rich

d) EDAX analysis of dark gray inclusion in center region: Al-rich

e) EDAX analysis of innermost inclusions: Al and S-rich.

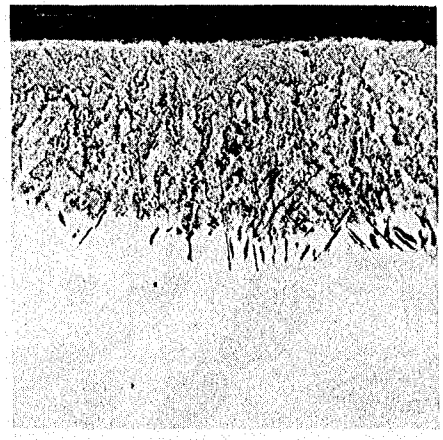

(a) Optical cross-section 50 μm

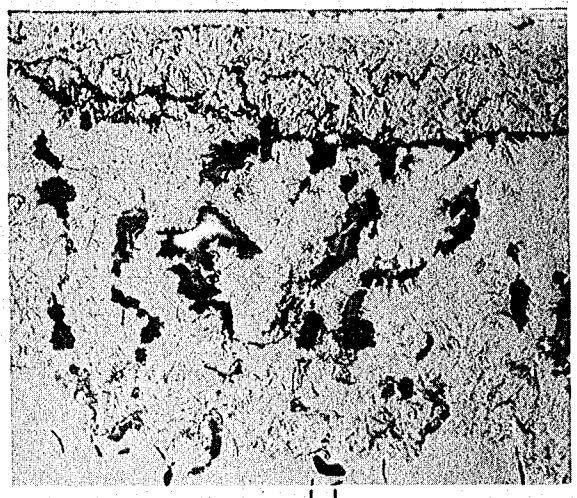

(b) Electron image 25 μm

EDAX analyses:

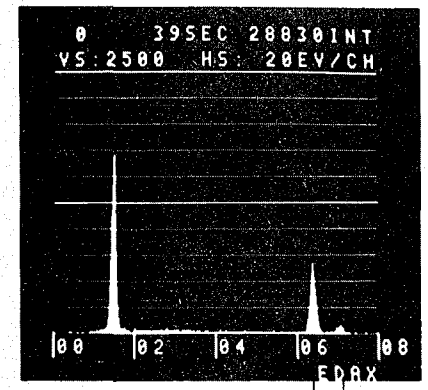

(c) Al Fe

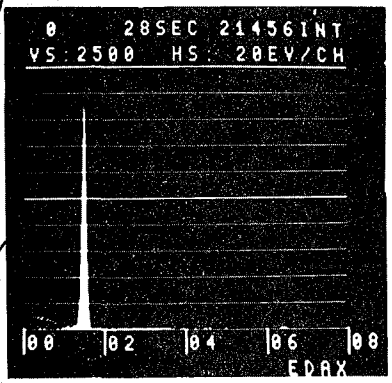

(d) Al

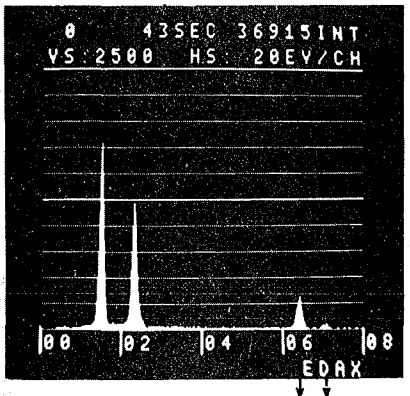

(e) Al S Fe

XBB 782-2453

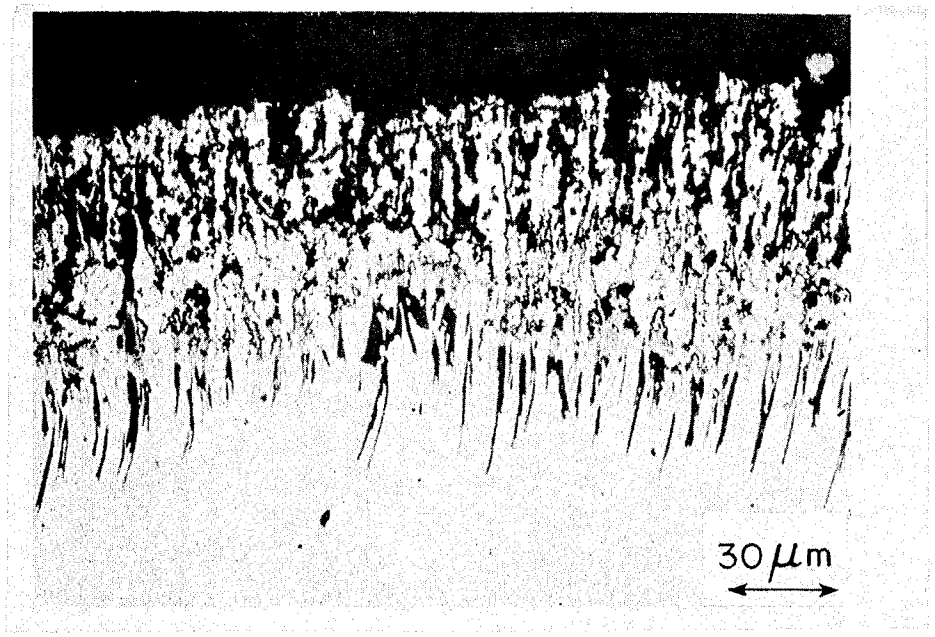

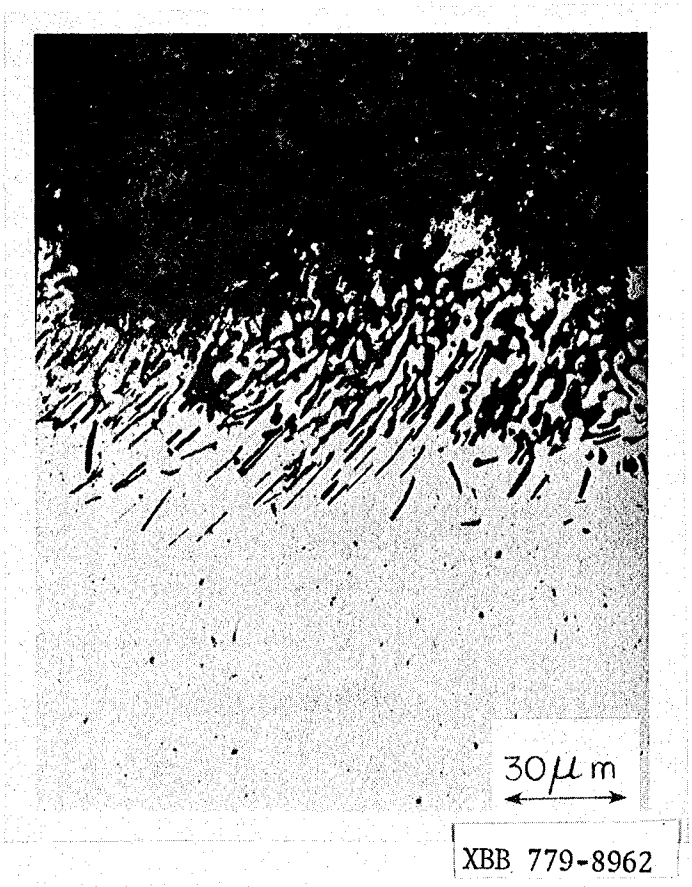

Figure 14. Optical micrographs of cross-sections of alloys from the screening tests (b) after 100 hours exposure in argon containing 6 to 10 ppm oxygen. (a) Fe-10Al . (b) Fe-10Al-5Cr . In both, the dark needles represent internal formation of aluminum-rich sulfides within the alloy itself. This region is covered by a scale which is predominantly iron oxide.

of aluminum and sulfur. Since that region is also rich in aluminum, such needles may consist of aluminum-rich sulfides. Figure 15 shows one such needle with Al and S x-ray maps. The two maps correspond to the extent that the long black needle in the center of the photomicrograph consists of Al and S . The other dark areas towards the top of the picture contain no sulfur although they are rich in aluminum.
Figure 16 shows a similar cross section and EDAX analysis of the scale formed on the Fe-10Al-5Cr alloy. Note that it is almost entirely Al_2O_3 . It is thin and dense with no visible microstructure and no evidence of internal penetration. The stainless steel alloys under all conditions used during these experiments showed only evidence of external Cr_2O_3 formation. The commercial 310 stainless steel with 1.0 - 1.5% Si showed the formation of internal silicon oxide inclusions (Figure 17). In spite of the appearance of these inclusions, the addition of silicon is used to improve oxidation resistance by serving as a getter for oxygen (29). In all of the tests performed, both of these alloys showed identical corrosion behavior: formation of external Cr_2O_3 layers and no internal penetration. Only the formation of the silicon oxide inclusions differentiated between the two. Exposure of the samples for 50 hours resulted in considerably less penetration on the Fe-10Al alloy, although the appearance of the penetrated region was identical to that observed after 100 hours exposure.

When the samples were exposed to the same environment for 50 and 100 hours at 871°C, no penetration was observed on any of the alloys, only the formation of a thin Al_2O_3 scale on the Fe-10Al and Fe-10Al-15Cr alloys. Both 310 stainless steels formed Cr_2O_3 layers identical in appearance and composition to those formed at 982°C.

Figure 15. Photomicrograph and X-ray maps of sulfur containing inclusion on Fe-10Al exposed to coal char for 100 hours at 982°C in pure CO.

a) Scanning electron photomicrograph

b) Aluminum X-ray map

c) Sulfur X-ray map

Note that inclusion is aluminum and sulfur rich while other inclusions are aluminum-rich.

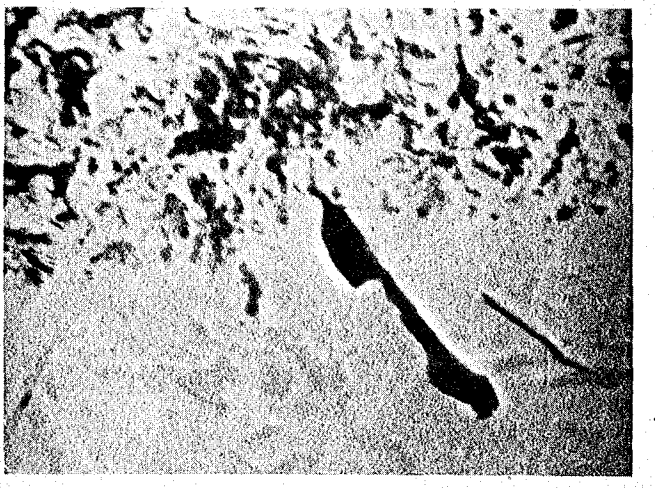

5 μm

(a) Electron image

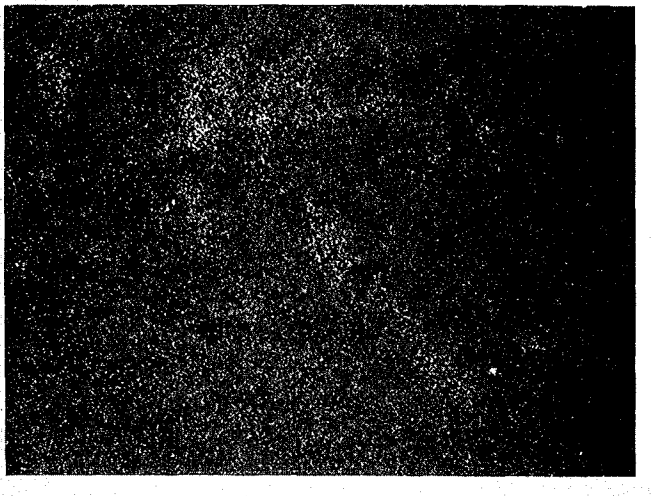

(b) Al x-ray map

(c) S x-ray map

XBB 782-2467

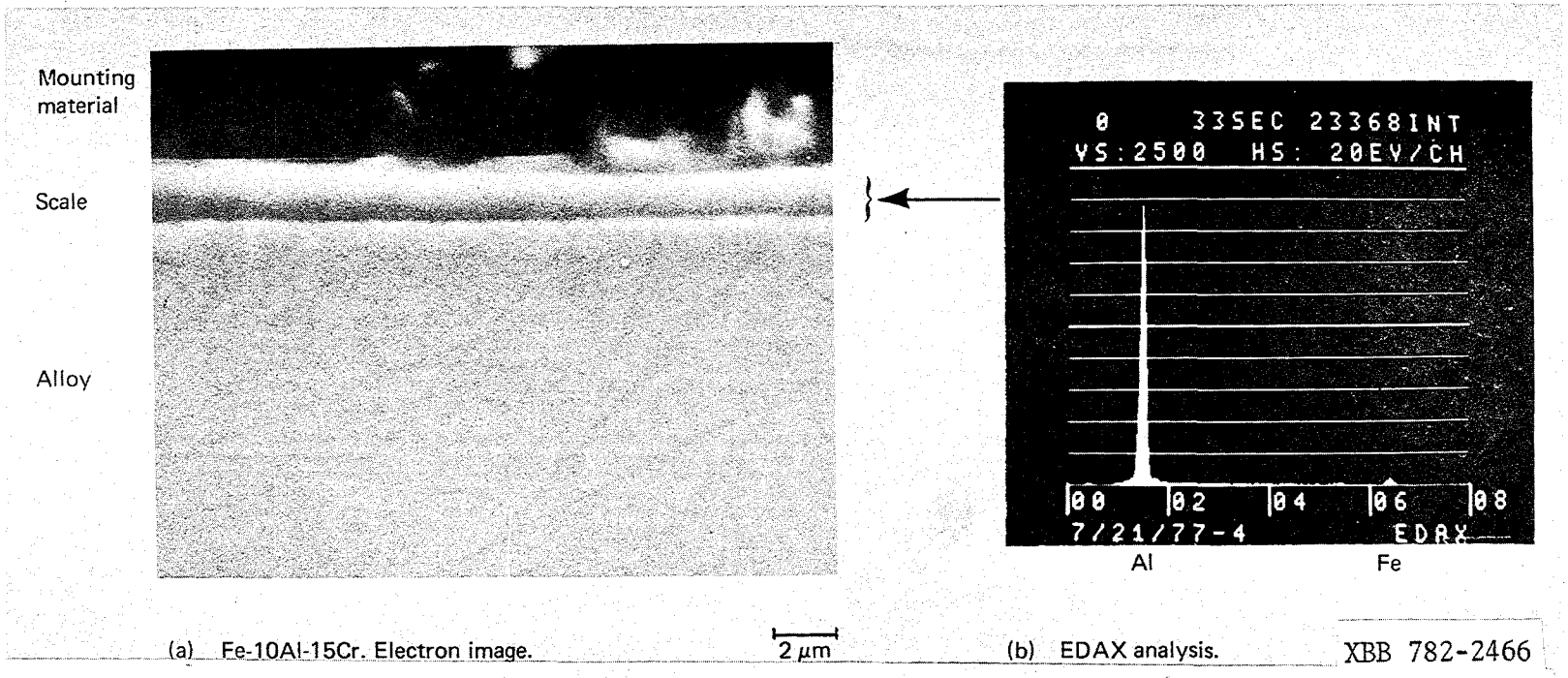

Figure 16. Cross section of scale formed on Fe-10Al-15Cr exposed to coal char for 100 hours at 982°C in pure CO .

a) Scanning electron image. Note thin, dense scale

b) EDAX analysis. Scale is Al_2O_3 .

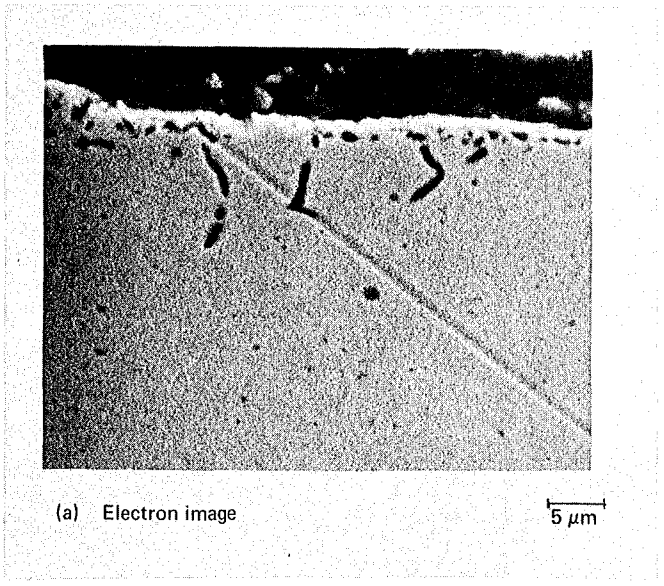

Figure 17. Cross section of scale formed on commercial 310 stainless steel exposed to coal char for 100 hours at 982°C in pure CO .

a) Electron image

b) High magnification of silicon-rich inclusion

c) EDAX analysis of inclusion

The samples were exposed to pure Al_2O_3 in CO/CO_2 at 982°C, and Figures 18-20 show that all of the alloys form adherent protective scales. Figure 18a-c shows the scale and the EDAX analysis for both Fe-10Al and Fe-10Al-15Cr . The Al_2O_3 scale shows up as a dark grey region spread uniformly over the alloy. The small trace of iron present is due to the uncertainty of penetration depth inherent in x-ray analysis and not to the presence of Fe in the scale. Figure 19a,b shows the pure 310 stainless steel and its EDAX analysis. The light grey scale is Cr_2O_3 with some Al present, probably from the Al_2O_3 powder to which the alloy was exposed. The commercial 310 alloy also develops a Cr_2O_3 scale, but as Figure 20a-c shows, it contains silicon oxide inclusions. As stated previously, only these inclusions differentiate between the commercial and pure melts of 310 stainless steel. There is, then, no attack by Al_2O_3 on any of the alloys. Thus any attack that is observed in the other tests must be from the sulfur-containing species.

If the overall morphologies of attack by the FeS-containing mixture (FeS-char) and the $CaSO_4$-containing mixture ($CaSO_4$-char) are examined, some important observations can be made. At low oxygen partial pressures $P_{O_2} = 10^{-19}$, $CaSO_4$ is much more reactive than FeS . Figure 21 shows the relative extent of attack by the two. Note that attack by the $CaSO_4$-char is massive and has affected a large portion of the surface of the Fe-10Al alloy. Attack by the FeS-char, even at a temperature above the melting point of the FeS-FeO eutectic appears to be confined to the formation of a thick, largely non-adherent scale. Analysis of this scale (Figure 22) shows it to be primarily Al_2O_3 . The scale resulting from $CaSO_4$ attack is more complex,

Figure 18. Cross-section of Fe-10Al and Fe-10Al-15Cr exposed to pure Al_2O_3 at 982°C for 50 hours in 38.4% CO + 61.6% CO_2 plus EDAX analysis.

a) Fe-10Al electron image

b) Fe-10Al-15Cr electron image

Note that both scales are identical Al_2O_3 layers with that on the Fe-10Al being slightly thicker.

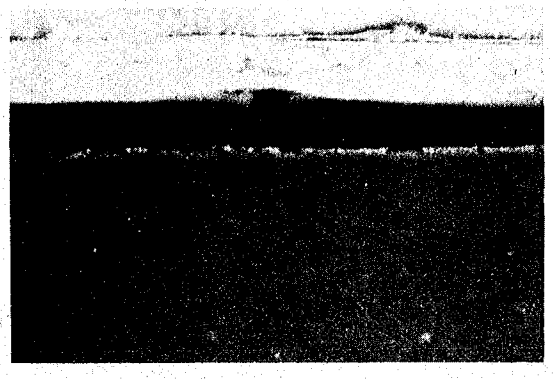

Region of EDAX analysis

(a) Fe-10Al electron image

5 μm

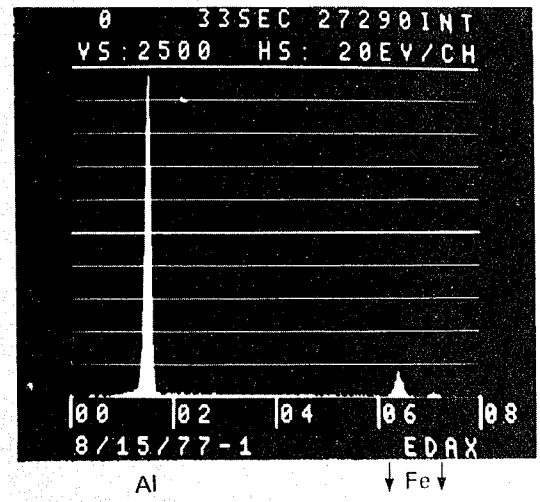

(c) EDAX analysis

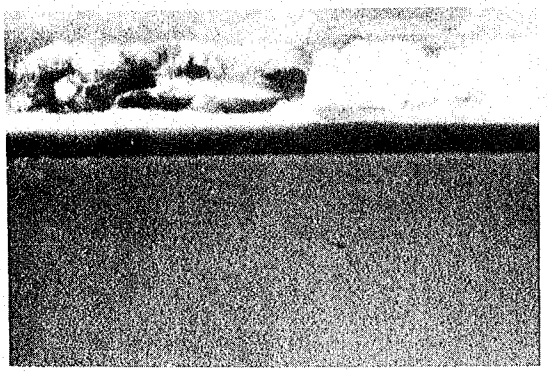

Region of EDAX analysis

(b) Fe-10Al-15Cr electron image

5 μm

XBB 782-2455

Figure 19. Cross section of pure 310 stainless steel exposed to pure Al_2O_3 at 982°C for 50 hours in CO/CO_2 mixture.

a) Electron image. Note thin, adherent Cr_2O_3 scale

b) EDAX analysis of scale.

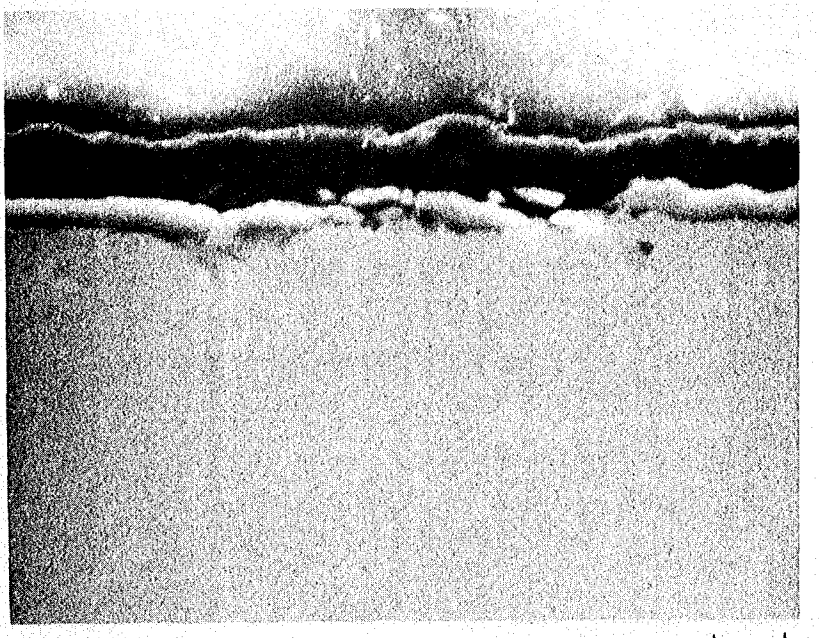

(a) Electron image

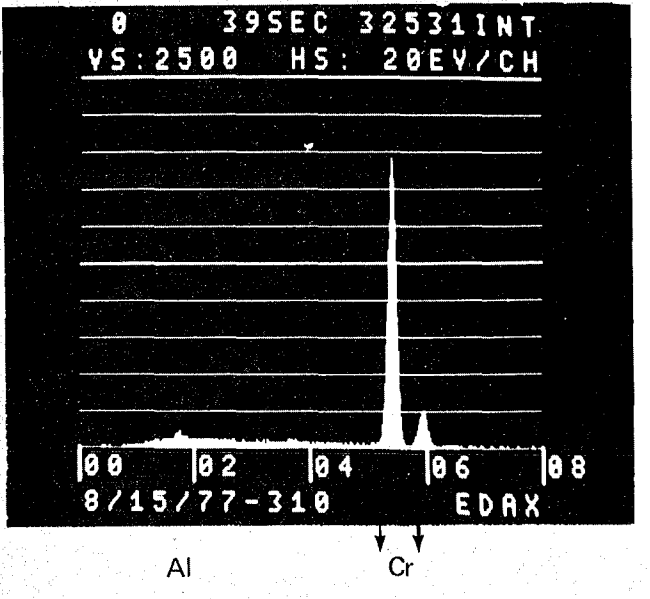

(b) EDAX analysis

XBB 782-2460

Figure 20. Cross section of commercial 310 s.s. exposed to pure Al_2O_3 at 982°C for 50 hours in CO/CO_2 mixture.

a) Electron image showing thin, adherent Cr_2O_3 scale

b) High magnification of inclusions

c) Silicon x-ray map of inclusions.

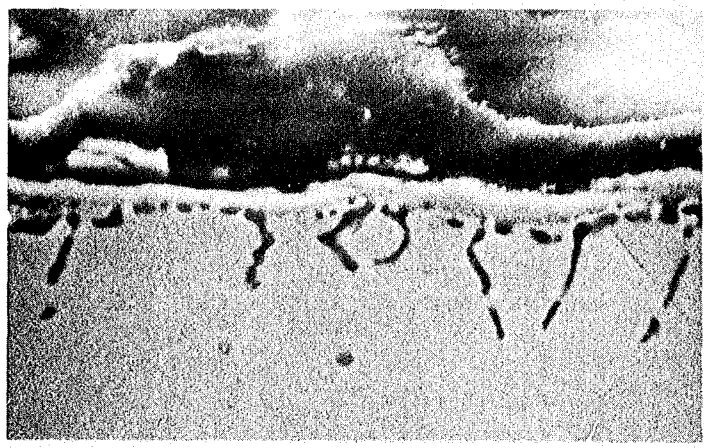

(a) Commercial 310 stainless steel — 5 μm

(b) High magnification of (a) — 2 μm

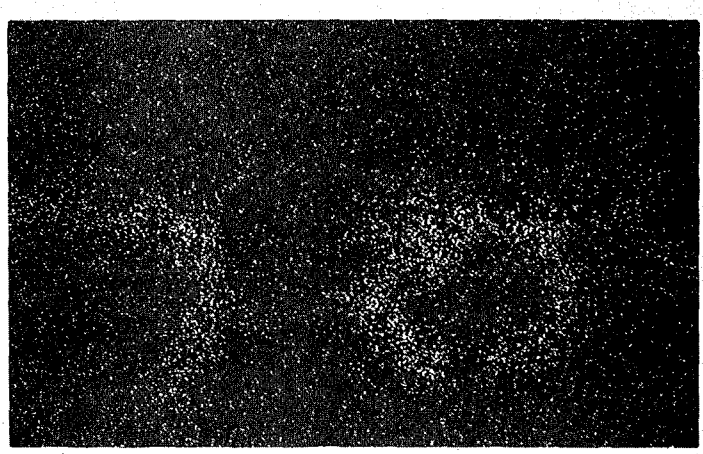

(c) Si x-ray map of (b)

XBB 782-2459

Figure 21. Fe-10Al exposed to synthetic char mixtures for 50 hours at 982°C and a $P_{O_2} = 10^{-19}$ atmosphere.

a) Sample in $CaSO_4$ containing mixture ($CaSO_4$-char)

b) Sample in FeS-containing mixture (FeS-char). The heavy black layer in (b) is an Al_2O_3 layer containing sufficient graphite and FeS to give it a dark appearance. Note the extensive scaling in (a) that does not appear in (b).

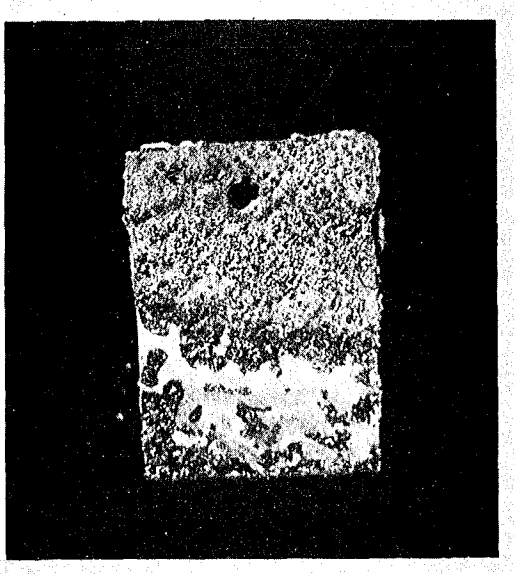

(a) Fe-10Al in $CaSO_4$-char.

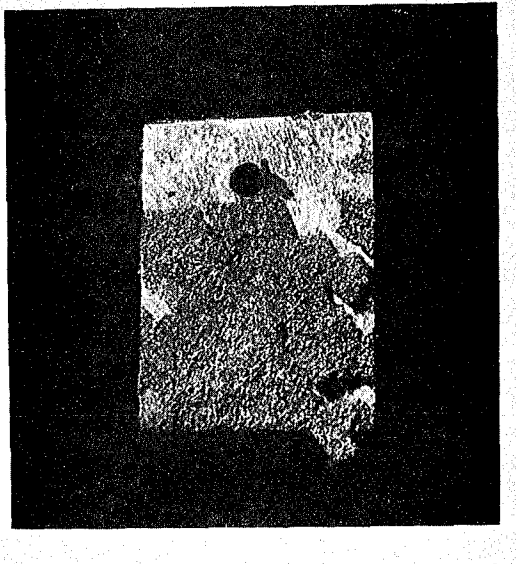

(b) Fe-10Al in FeS-char.

XBB 782-2474

Figure 22. Fe-10Al exposed to FeS-char for 50 hours at 982°C and a $P_{O_2} = 10^{-19}$ atmosphere.

a) Electron image

b) EDAX analysis of scale

Note that the EDAX analysis shows scale to be Al_2O_3.

(a) Fe-10Al in FeS-char.

0.5 mm

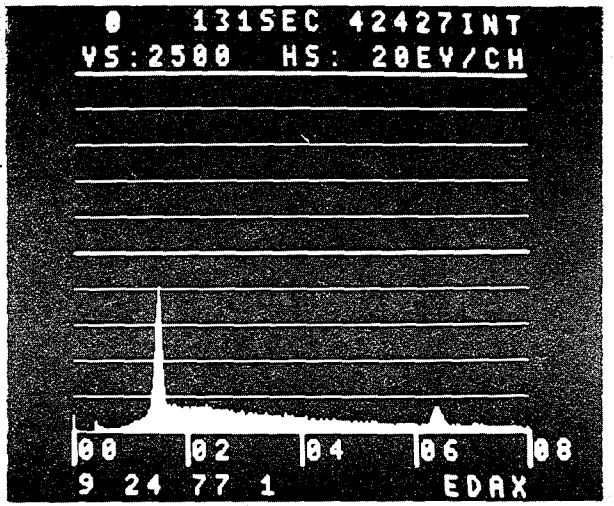

Al Fe

(b) EDAX analysis.

XBB 782-2471

consisting of a large amount iron-rich oxides. Figure 23a shows the scale to be thick with cancer-like growths. Under high magnification, these take on the appearance of rope-like extrusions and consist almost entirely of iron as iron oxide (Figure 23c). Although the appearance is quite different from the scale formed under char in the preliminary experiments, the chemical analysis is almost identical. A cross-section of this scale is shown in Figure 24a, revealing extensive external growth and internal penetration. Under high magnification, the scale region has a two-phase microstructure (Figure 24b) which x-ray mapping shows is made up of iron-rich and aluminum-rich regions (Figures 24c and d). Figure 25 shows that at the innermost limit of attack there are a number of small but identifiable aluminum-rich sulfide inclusions, reminiscent of char attack.

Scale formation on the other three alloys was confined to formation of Al_2O_3 or Cr_2O_3 layers with no internal penetration. Under similar conditions at 871°C, no internal attack was observed on any of the alloys, including the Fe-10Al alloy. This pattern was observed in all of the runs at 871°C except where specified otherwise.

Where no significant morphologies were observed, the results are not explicitly discussed. For example, after 50 hours exposure at 982°C to coal char, the morphology of the corrosion observed on the Fe-10Al alloy was identical in all respects to that observed after 100 hours. It was, however, confined to localized regions rather than the entire alloy surface. Table 9 at the end of chapter 3 references the figures in which specific results are shown. Where there are no figure references, no significant results were observed.

Figure 23. Fe-10Al exposed to $CaSO_4$-char for 50 hours at 982°C and a $P_{O_2} = 10^{-19}$ atmosphere.

a) Overall electron image of scale

b) High magnification of scale

c) EDAX analysis of scale

Note spaghetti-like structure of scale and the composition, which appears to iron oxide, possibly FeO .

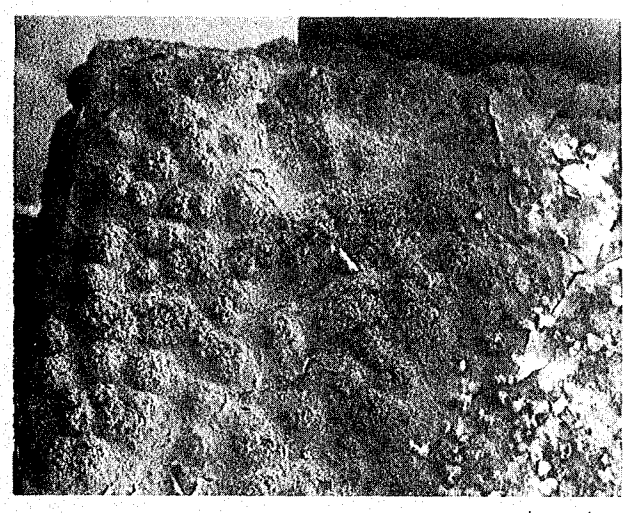

(a) Fe-10Al in $CaSO_4$-char. 0.5 mm

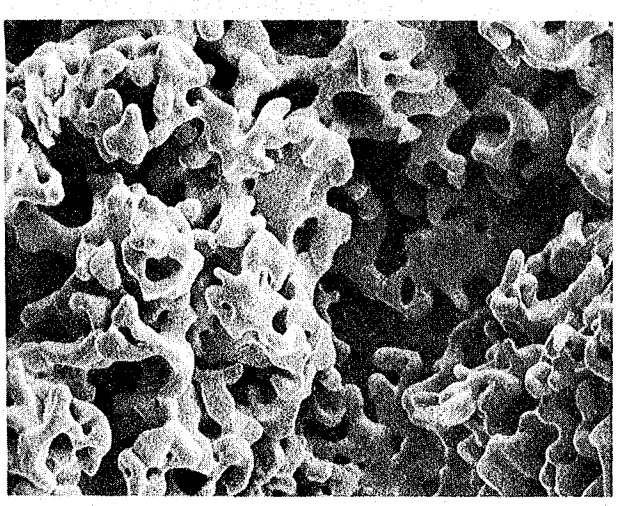

(b) High magnification of (a) 20 μm

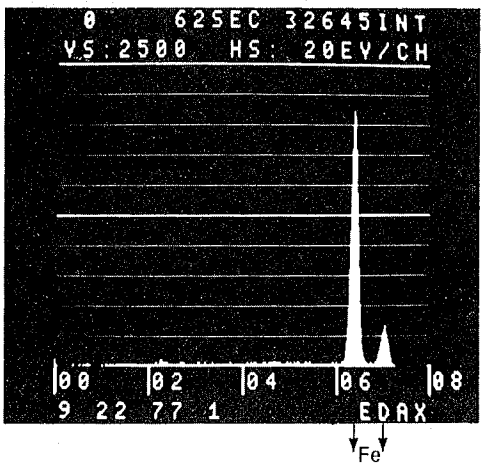

(c) EDAX analysis.

XBB 782-2461

Figure 24. Cross section of Fe-10Al exposed to $CaSO_4$-char for 50 hours at 982°C and a $P_{O_2} = 10^{-19}$ atmosphere.

a) Overall electron image of scale. Protrusions are polishing particles that have been imbedded in the scale

b) High magnification of two-phase region

c) Aluminum X-ray map

d) Iron X-ray map

Note that aluminum-rich regions correspond to iron-poor regions.

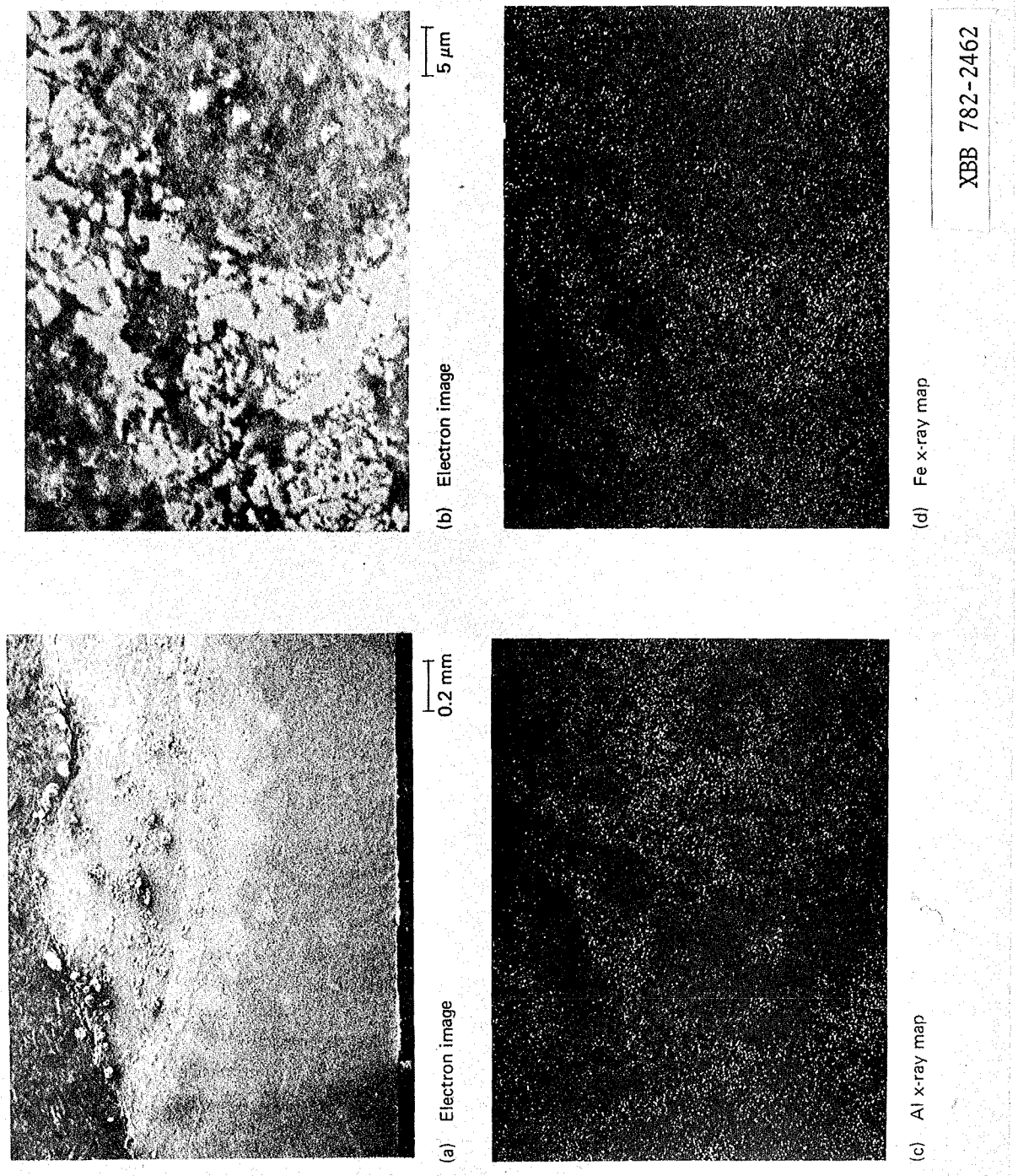
0.2 mm
5 μm
(a) Electron image
(b) Electron image
(c) Al x-ray map
(d) Fe x-ray map

XBB 782-2462

Figure 25. Cross section of Fe-10Al exposed to $CaSO_4$-char for 50 hours at 982°C and a $P_{O_2} = 10^{-19}$ atmosphere.

a) Electron image of sulfide containing-inclusions at alloy-scale interface

b) EDAX analysis of inclusions showing high aluminum and sulfur concentrations

Note that inclusions are round rather than needle-shaped.

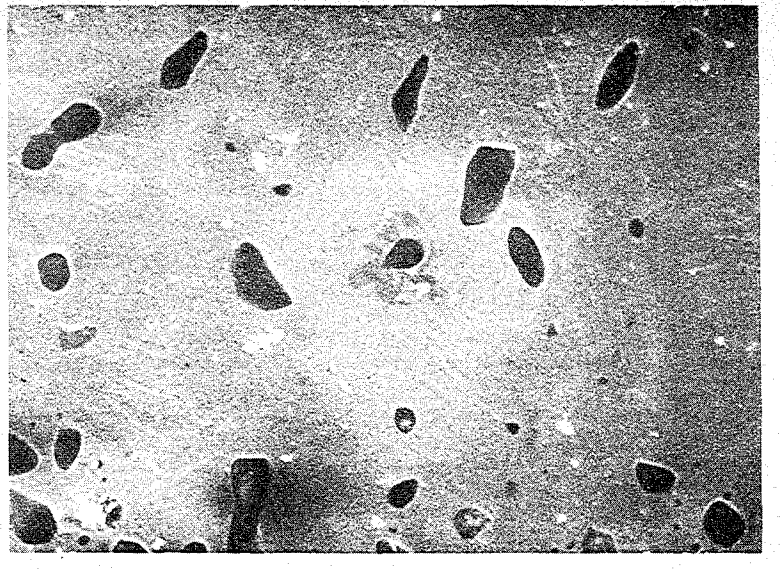

(a) Fe-10Al in $CaSO_4$-char.

10 μm

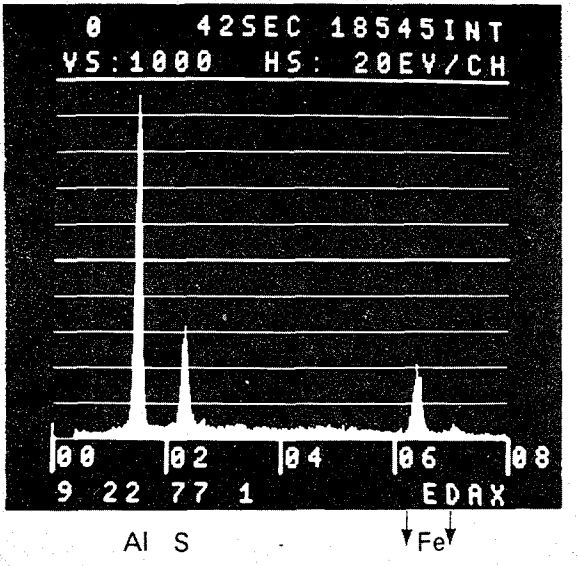

(b) EDAX of inclusions

XBB 782-2469

At the higher oxygen partial pressure ($\sim 4.2\times10^{-15}$ atmosphere) the situation is reversed. Attack by FeS is so aggressive that after 50 hours the Fe-10Al alloy had completely reacted, leaving behind a residue of Al_2O_3 and iron oxides. The effect of $CaSO_4$ on the Fe-10Al and Fe-10Al-5Cr alloys is shown in Figure 26. Both have obviously corroded but not nearly to the extent that occurs at the lower oxygen potential. It is interesting to note that the Fe-10Al-15Cr alloy also underwent fairly extensive attack, something which did not occur under any other set of conditions. The morphology of this attack is quite complicated (Figure 27). This figure shows a complex, multilayered scale on which are superimposed x-ray line scans. These line scans, for iron and aluminum, plot concentration as a function of position across the center of the photomicrograph. The protrusion plotted in Figure 27 consists of dark grey aluminum-rich regions and light grey iron-rich regions. The center region appears to be a uniform region of constant iron and aluminum composition and perhaps is an uncorroded piece of the alloy itself. This is the only sample which underwent internal attack in which no sulfur was observed.

Because exposure to FeS resulted in such rapid attack, tests were performed using only the Fe-10Al binary and exposures of 1, 2, and 5 hours (see Tables 7 and 8). Figure 28 graphically illustrates the rapidity with which the FeS-char induced attack spreads out from the edges and corners. After two hours the surface growths already begin to show a needle-like structure. EDAX analysis shows these peaks to be rich in sulfur and iron (Figure 29a,b). Under high magnification (2000x) an interesting microstructure shows up (Figure 30). Figure 30a shows the electron image. Note the two separate and distinct phases - one consisting of light grey stringers imbedded in the other.

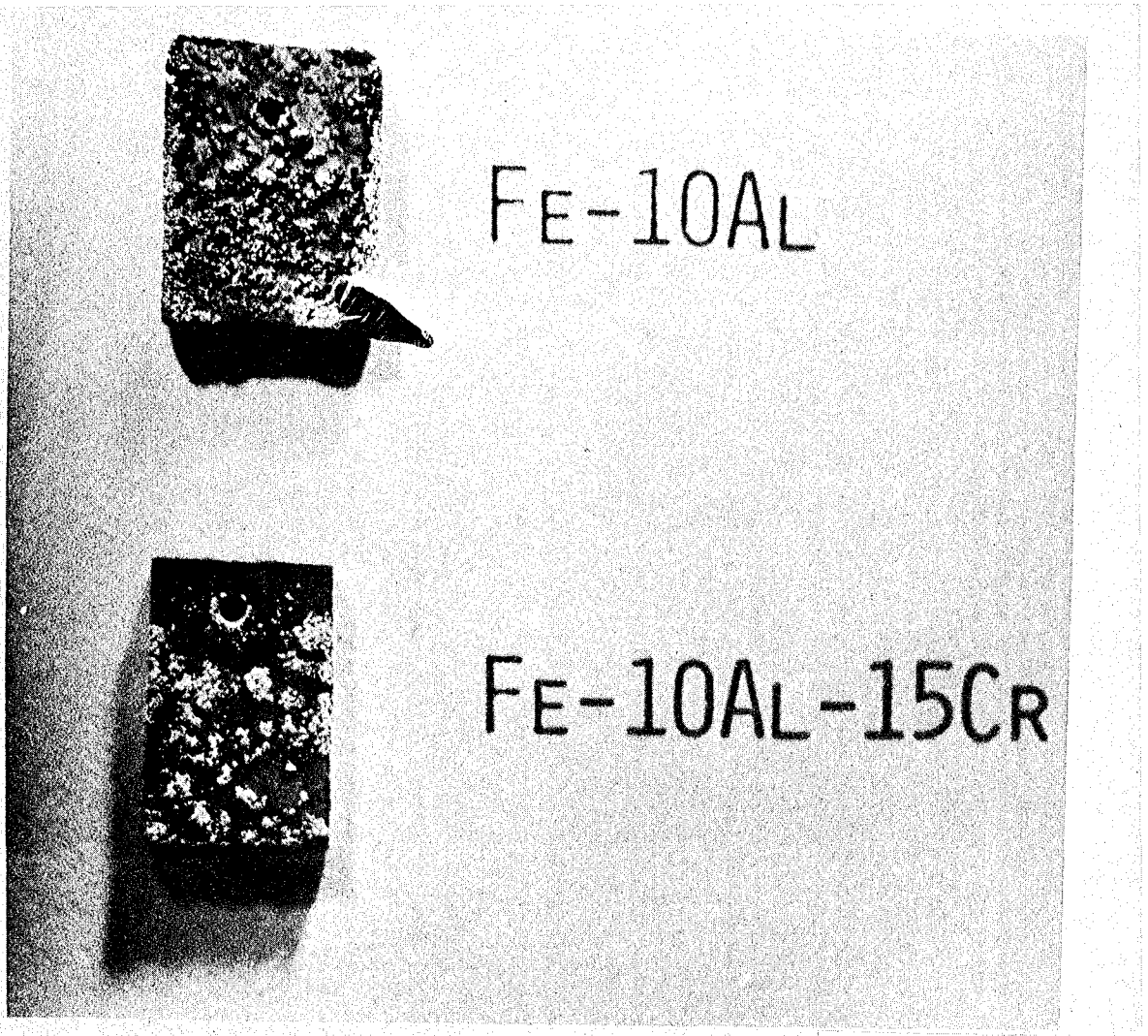

Figure 26. Surface macrophotographs of Fe-10Al and Fe-10Al-15Cr samples exposed to $CaSO_4$-char for 50 hours at 982°C and a $P_{O_2} = 4.2\times10^{-15}$ atmosphere. Note scaling on both alloys.

Figure 27. Cross section of protrusion on Fe-10Al-15Cr alloy exposed to $CaSO_4$-char for 50 hours at 982°C and a $P_{O_2} = 4.2 \times 10^{-15}$ atmosphere. X-ray line scans are superposed. Top: iron scan, bottom: aluminum scan. Note in particular that the dark grey regions are aluminum-rich and the light grey are iron-rich. Smooth uniform region appears to be unattached alloy.

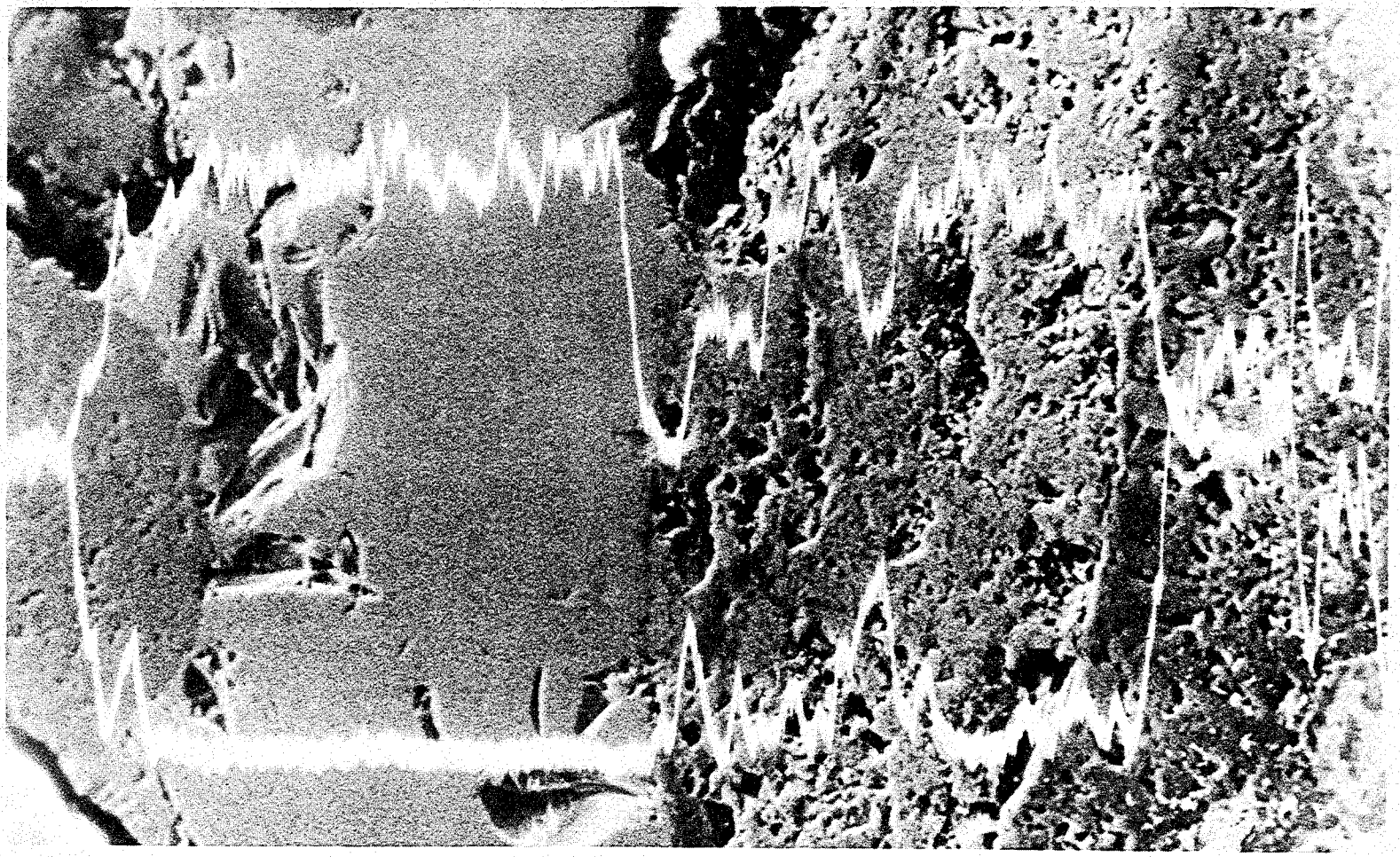

XBB 782-2464

Fe-10Al-15Cr in $CaSO_4$-char. Line scans across center of picture. Top – Fe scan. Bottom – Al scan.

Figure 28. Macrophotographs of Fe-10Al exposed to Fe-S-char at 982°C and a $P_{O_2} = 4.2 \times 10^{-15}$ atmosphere.

a) 1 hour exposure

b) 2 hour exposure

c) 5 hour exposure

Note rapidity with which attack spreads out over surface.

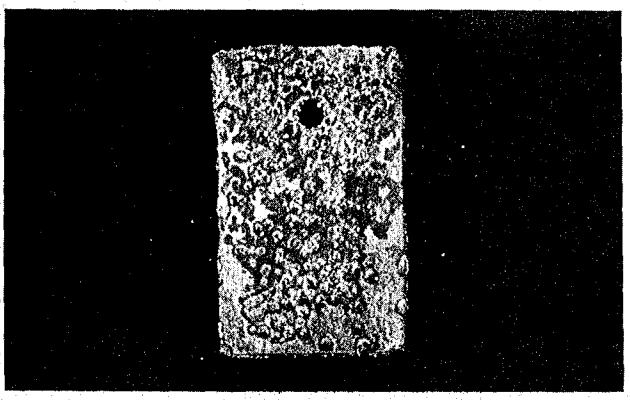

(a) Fe-10Al – 1 hour exposure

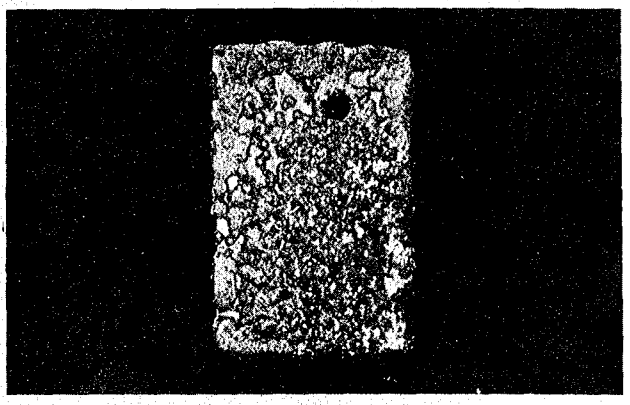

(b) Fe-10Al – 2 hour exposure

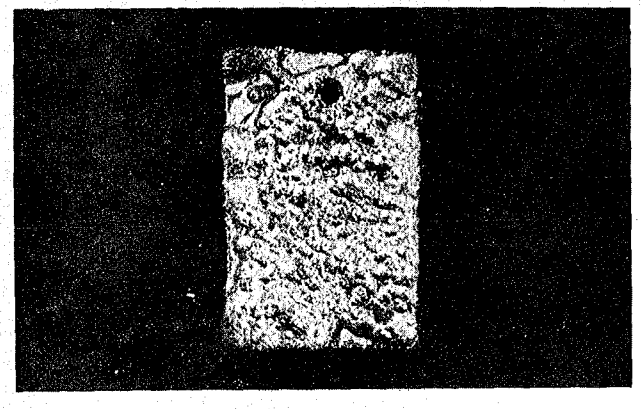

(c) Fe-10Al – 5 hour exposure

XBB 782-2456

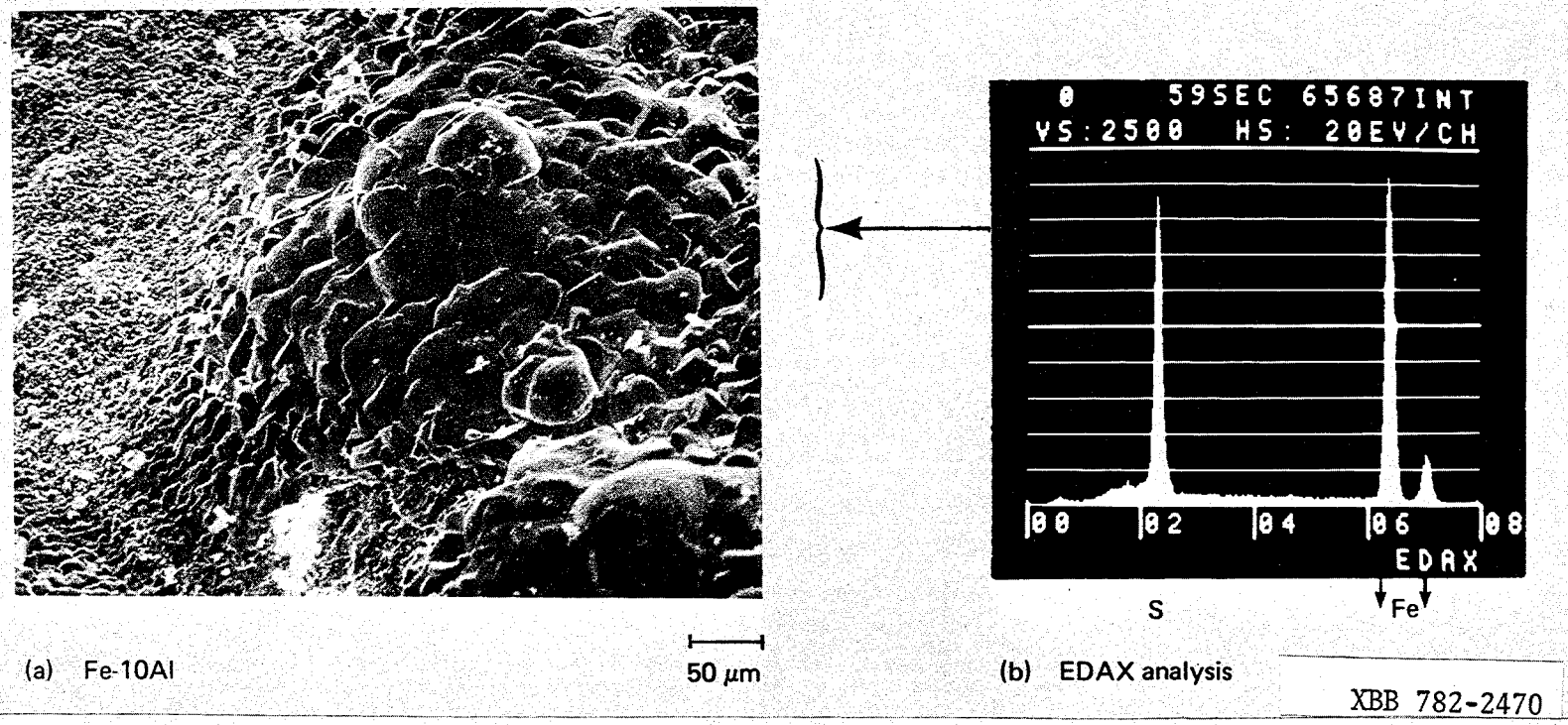

Figure 29. Fe-10Al exposed to FeS-char for 2 hours at 982°C and a $P_{O_2} = 4.2 \times 10^{-15}$ atmosphere.

a) Electron image of surface protrusion

b) EDAX analysis showing high sulfur concentration of peaks.

Figure 30. Fe-10Al exposed to FeS-char for 2 hours at 982°C and a $P_{O_2} = 4.2 \times 10^{-15}$ atmosphere.

a) Electron image of surface protrusion. Note smooth, molten appearance with needles of a second phase

b) Sulfur X-ray map shows needles are sulfur-rich

c) Iron X-ray map shows uniform iron concentration.

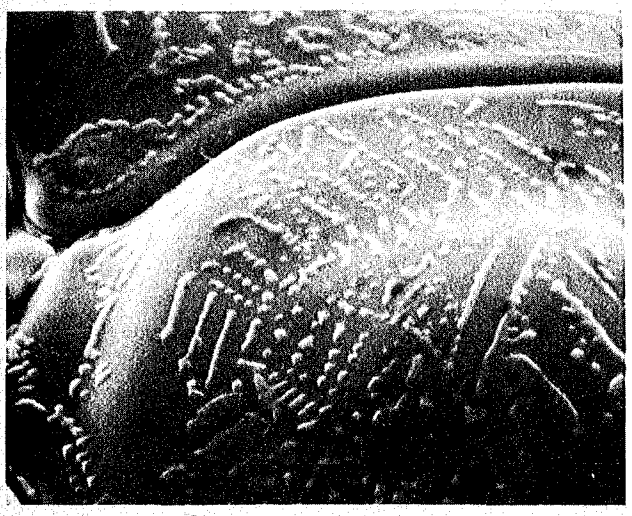

(a) Electron image

5 μm

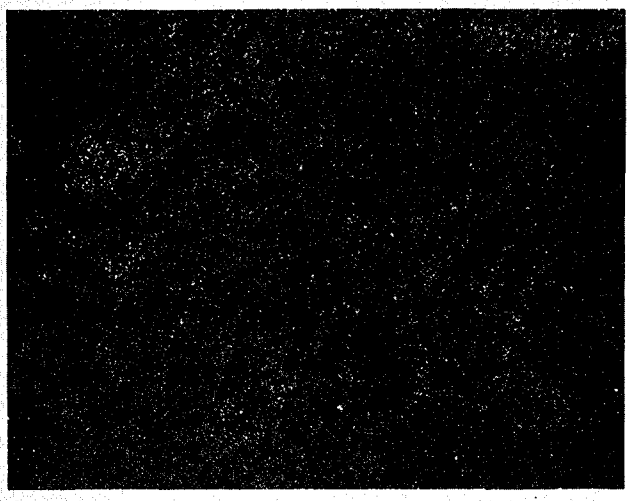

(b) S x-ray map

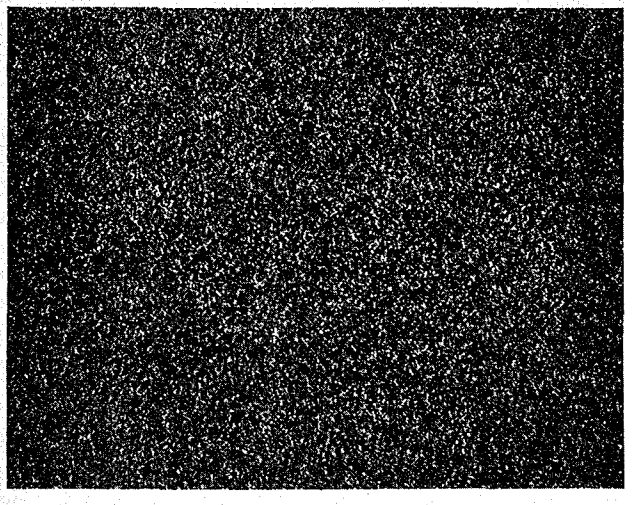

(c) Fe x-ray map

XBB 782-2457

Figures 30b,c show that these stringers are predominantly iron-rich sulfide, probably FeS . This structure is most likely due to oxidation of the sulfide and is typical of the formation of a eutectic.

On cross-sectioning, a familiar structure appears, seen in Figure 31. In Figure 31a, a multilayered scale structure is obvious, with long narrow dark grey stringers at the scale-alloy interface. Under high magnification (Figure 31b) and using the technique of x-ray mapping (Figures 31c-e), these stringers are recognizable as aluminum-rich sulfides, similar in appearance to those in Figure 14.

Thus far, most of the discussion has involved corrosion at 982°C. This is because the attack is most rapid at this temperature, and the results are easier to observe. A brief discussion will give an idea of the relative magnitudes of the attack. Figures 32 and 33 show macrophotographs of eight samples exposed for 50 hours at 871°C. Figure 32 shows those in FeS at $P_{O_2} = 4.8\times10^{-17}$, and Figure 33 shows those in $CaSO_4$ at $P_{O_2} = 4.8\times10^{-17}$. Both sets show considerably less attack than at the higher temperature, with the FeS char-exposed alloys showing virtually no surface scaling and, on cross-sectioning, no penetration except for thin Al_2O_3 or Cr_2O_3 layers. The $CaSO_4$ char-exposed samples, however, do show some external growths on the Fe-10Al and Fe-10Al-15Cr alloys, reminiscent of those in Figure 21a. At a higher magnification (Figure 34), the surface protrusions on the Fe-10Al alloy turn out to be iron- and sulfur- rich and aluminum-poor while the surrounding scale is predominantly Al_2O_3 . Cross-sectioning reveals no internal penetration except on the Fe-10Al-15Cr alloy which, as Figure 35 shows, has a small amount of penetration by sulfur. Figure 35c shows the dark grey regions contain some aluminum-rich

Figure 31. Cross section of Fe-10Al exposed to FeS-char for 2 hours at 982°C and a $P_{O_2} = 4.2 \times 10^{-15}$ atmosphere.

a) Electron image of corroded alloy. Note needles at alloy/scale interface

b) High magnification of (a)

c) Sulfur X-ray map

d) Aluminum X-ray map

e) Iron X-ray map

Note that needles are aluminum and sulfur-rich. Figure is inverted from normal orientation, i.e., scale is at bottom of image.

(a) Fe-10Al. Electron image

50 μm

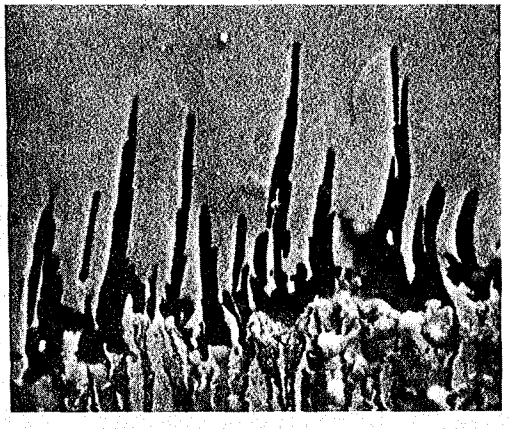

(b) Electron image

5 μm

(c) S x-ray map

(d) Al x-ray map

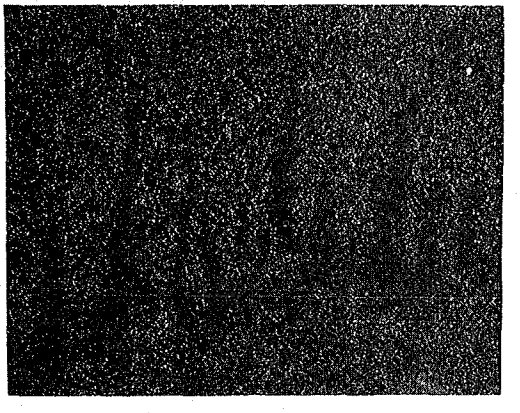

(e) Fe x-ray map

XBB 782-2454

Figure 32. Samples exposed to FeS-char for 50 hours at 871°C and a $P_{O_2} = 4.8 \times 10^{-17}$.

a) Fe-10Al

b) Fe-10Al-15Cr

c) Pure 310 stainless steel

d) Commercial 310 stainless steel

Note relative lack of scaling.

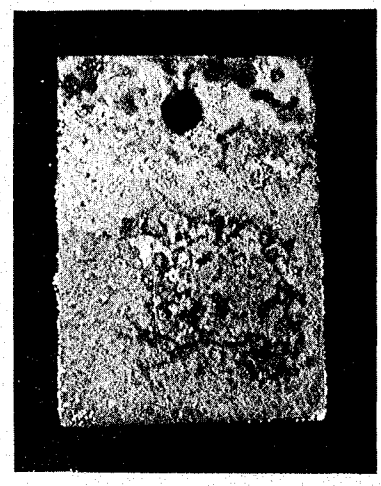

(a) Fe-10Al

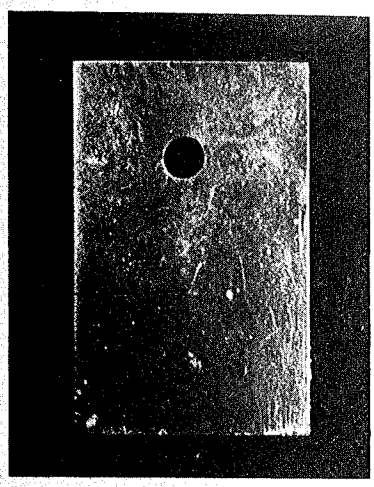

(b) Fe-10Al-15Cr

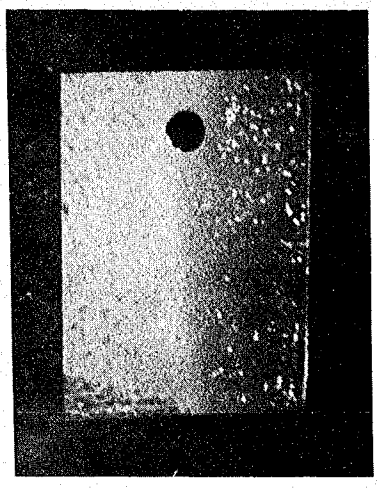

(c) Pure 310 s.s.

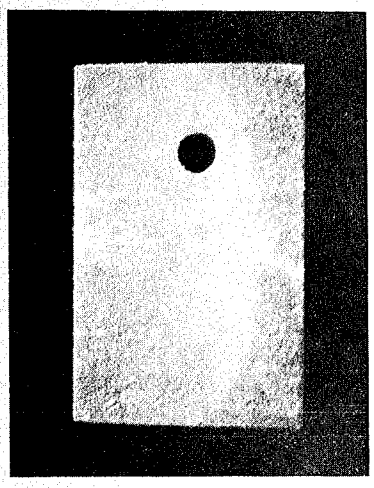

(d) Commercial 310 s.s.

XBB 782-2473

Figure 33. Samples exposed to $CaSO_4$-char for 50 hours at 871°C and a $P_{O_2} = 4.8 \times 10^{-17}$.

a) Fe-10Al

b) Fe-10Al-15Cr

c) Pure 310 stainless steel

d) Commercial 310 stainless steel

Note occasional protrusions but overall lack of corrosion.

(a) Fe-10Al

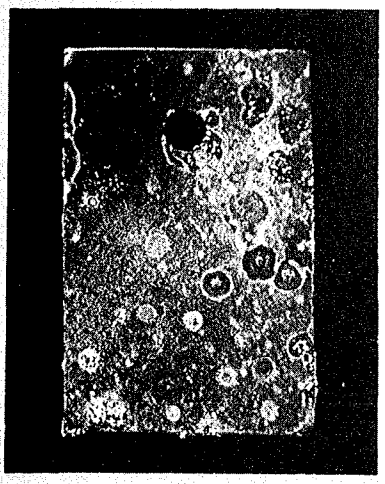

(b) Fe-10Al-15Cr

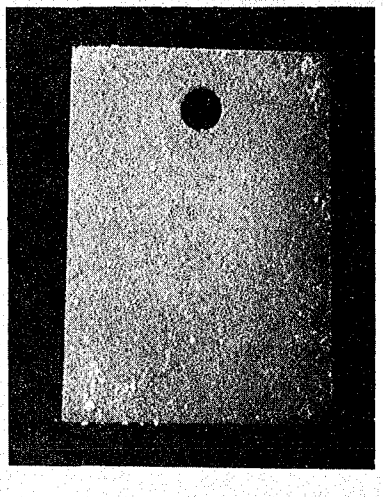

(c) Pure 310 s.s.

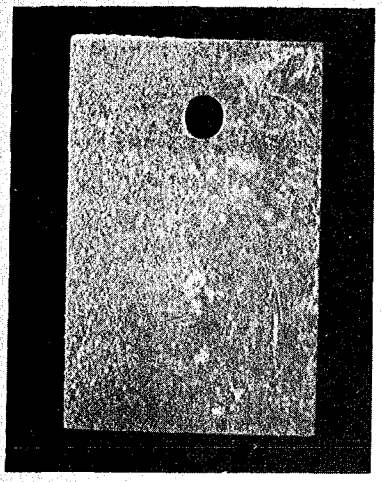

(d) Commercial 310 s.s.

XBB 782-2472

Figure 34. Fe-10Al exposed to $CaSO_4$-char for 50 hours at 871°C and a $P_{O_2} = 4.8 \times 10^{-17}$ atmosphere.

a) Electron image

b) Sulfur X-ray map

c) Aluminum X-ray map

d) Iron X-ray map.

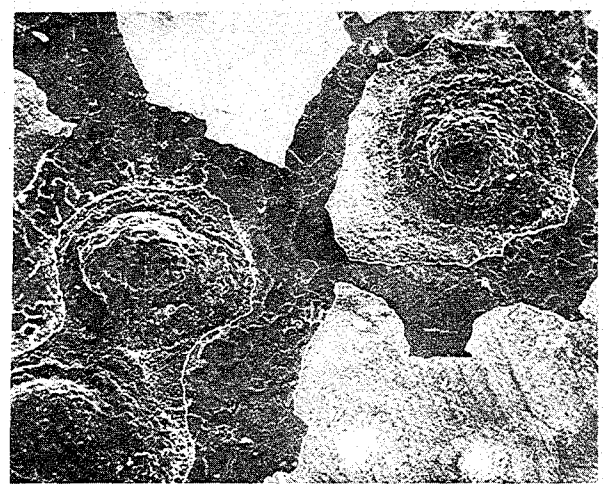

(a) Fe-10Al. Electron image

100 μm

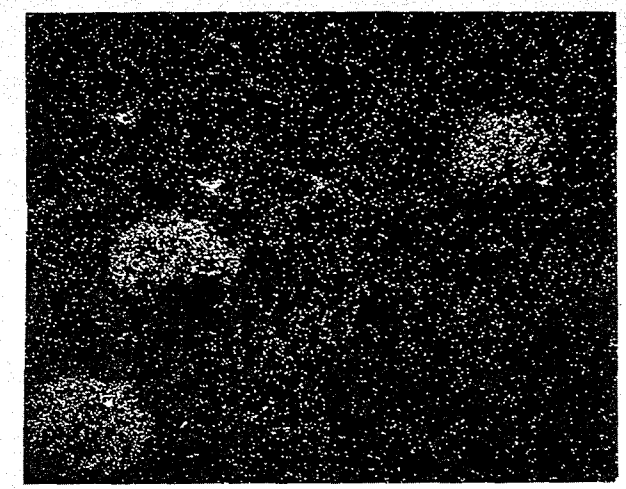

(b) S x-ray map

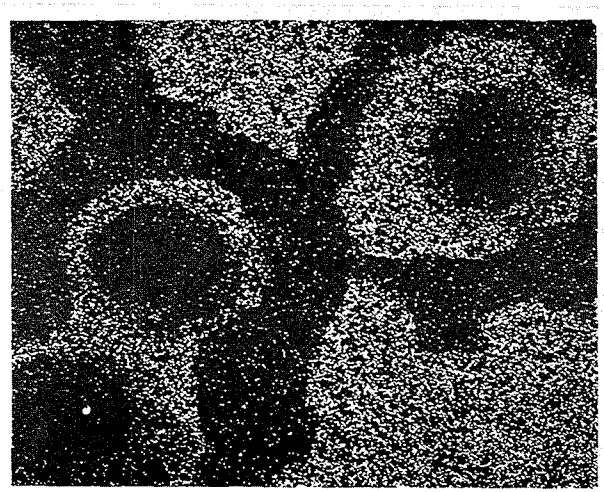

(c) Al x-ray map

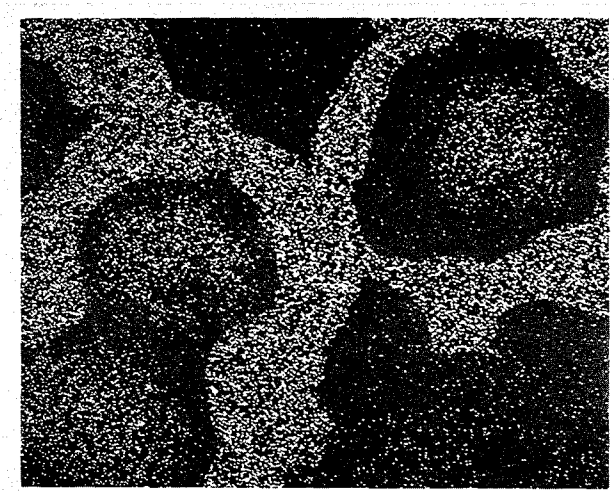

(d) Fe x-ray map.

XBB 782-2458

Figure 35. Cross section of Fe-10Al-15Cr alloy exposed to $CaSO_4$-char for 50 hours at 871°C and a $P_{O_2} = 4.8 \times 10^{-17}$ atmosphere.

a) Electron image. Note dark grey inclusions

b) EDAX Analysis of inclusions shows them to be aluminum and sulfur rich with a trace of calcium

c) EDAX of bulk alloy.

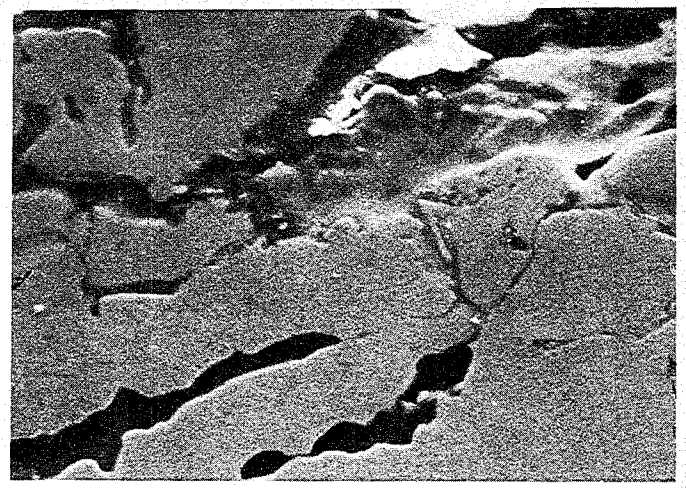

(a) Fe-10Al-15Cr in $CaSO_4$-char. 10 μm

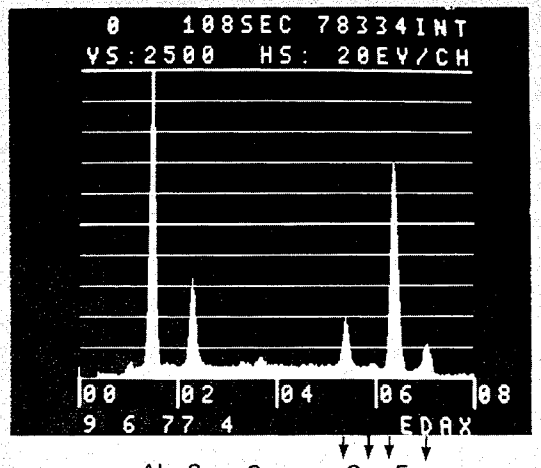

(b) EDAX of grey inclusion.

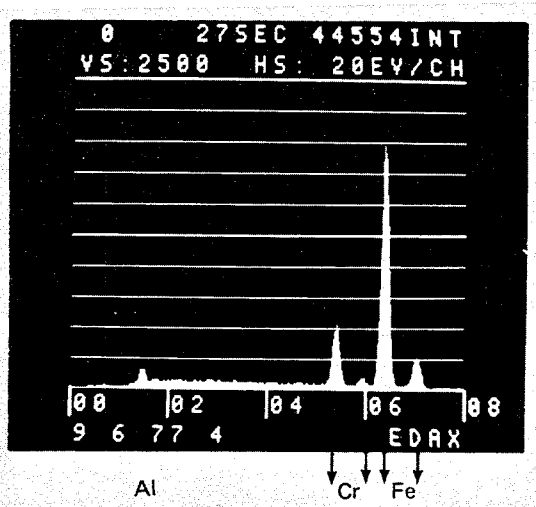

(c) EDAX of bulk alloy.

XBB 782-2468

sulfides, but there are none of the sulfide inclusions observed on the alloys exposed to $CaSO_4$-char at 982°C. There also were none of the needle-shaped inclusions of aluminum-rich sulfides that were observed following exposure to either coal-char at a low P_{O_2} or FeS at a high P_{O_2}, both at 982°C. Those were similar in morphology and composition to the sulfide inclusions observed in the screening runs.

Table 9 gives a summary of the experimental conditions to which the alloys were and the figures in which they are represented. Except as indicated, the low temperature runs were not discussed because scaling was confined to formation of Al_2O_3 or Cr_2O_3 layers.

Table 9. Matrix of results discussed.

Char or Substitute	P_{O_2}	Temp.	Time	Fe-10Al	Fe-10Al-15Cr	310 s.s. pure	310 s.s. comm.
Screening runs (char)	very high	982	24,100	3,14	3*,4*,14*		
Coal char	low	982	100	13,15	16		17
Coal char	low	982	50				
Coal char	low	871	100				
Coal char	low	871	50				
Pure Al_2O_3	high	982	50	18	18	19	20
FeS	high	982	50				
$CaSO_4$	high	982	50	26	26,27		
FeS	high	982	1,2,5	28,29,30,31			
FeS	high	871	50	32	32	32	32
$CaSO_4$	high	871	50	33,34	33,35	33	33
FeS	low	982	50	21,22			
FeS	low	871	50				
$CaSO_4$	low	982	50	21,23,24,25			
$CaSO_4$	low	871	50				

*Fe-10Al-5Cr in screening runs only.

CHAPTER 4

Discussion and Conclusions

A. Effects of Char Composition on Scale

Table 10 shows a summary of the experimental results at 982°C. There is sufficient sulfur present in coal char to result in the active sulfidation of iron-base alloys (Figures 13-15). Even at low oxygen partial pressures, ample penetration occurred on the Fe-10Al alloy. The morphology of the attack was similar to that from the preliminary screening runs although not nearly as extensive. This attack is characterized by needles of aluminum-rich sulfides at the alloy/scale interface with a region of Al_2O_3 penetration behind this scale (Figure 13b). Finally, there is usually a region of oxide penetration in which the oxide inclusions contain both iron and aluminum, possibly an iron-aluminum spinel. The indication is that a specific, reproducible pattern of attack is responsible for char-induced corrosion. This pattern may depend on the availability of sulfur at the specific conditions as well as the species responsible for the sulfur. In order to determine what species is primarily responsible for this corrosion, the same mode of attack should be observed.

Those synthetic chars containing 5 mole% $CaSO_4$ resulted in extensive attack at a calculated oxygen partial pressure of $\leq 10^{-19}$ atmosphere and less substantial attack at higher P_{O_2}'s . This attack shows a moderately similar morphology to attack by coal char. Cross-sectioning shows inclusions of aluminum-rich sulfides (Figure 25), while the surface analysis shows a predominance of iron oxide (Figure 23). Both of these have been observed on iron-base alloys

Table 10. Summary of experimental results at 982°C.

		Fe-10Al	Fe-10Al-15Cr	pure 310 s.s. Fe-25Cr-20Ni	commercial 310 s.s.
FeS	low P_{O_2}	Al_2O_3 scale	Al_2O_3 scale	Cr_2O_3 scale	Cr_2O_3 scale Si-rich inclusions
	high P_{O_2}	heavy FeS-FeO scale, extensive sulfide inclusions	Al_2O_3 scale	Cr_2O_3 scale	Cr_2O_3 scale Si-rich inclusions
$CaSO_4$	low P_{O_2}	heavy FeO scale some sulfide inclusions	some surface scaling	Cr_2O_3 scale	Cr_2O_3 scale Si-rich inclusions
	high P_{O_2}	some surface scaling and penetration	light surface scaling and penetration	Cr_2O_3 scale	Cr_2O_3 scale Si-rich inclusions
Coal Char	low P_{O_2}	light scaling extensive penetration-some S	Al_2O scale	Cr_2O_3 scale	Cr_2O_3 scale Si-rich inclusions
	high P_{O_2} (screening expt.)	massive FeO scale sulfide inclusions	not tested	not tested	Cr_2O_3 scale Si-rich inclusions

in coal char, but the appearance is different. From coal char, the sulfide inclusions are long and needle-shaped (Figures 13a, 15) and the surface layer of iron oxide (probably FeO from thermodynamic considerations but no quantitative analysis was performed to determine the precise composition) is smooth and appears to have been molten. On the other hand, the sulfide inclusions from the $CaSO_4$-char are round, and the surface layer of FeO has a rough, spaghetti-like appearance.

Corrosion resulting from contact with synthetic char containing 5 mole% FeS has a decidedly different appearance although a similar morphology to that from $CaSO_4$-char. The scale grows very rapidly at an oxygen potential of approximately 10^{-15} atmosphere, and after a few hours (Figure 28) begins to develop a smooth, molten appearance. These smooth protrusions have an iron-rich composition and in the early stages contain a large amount of sulfur. They obviously come from FeS on the alloy surface and, as Figure 30 shows, they develop a eutectic structure from oxidation of the sulfide. Once the FeS-FeO eutectic is formed, the scale can melt as its melting point decreases, and a more intimate contact with the alloy surface is possible. This probably serves to increase the rate of attack.

The cross-sectioning of the alloys reveals additional similarities between the corrosion morphologies of coal char-induced and FeS-char induced corrosion. The appearance of long thin needles consisting of aluminum-rich sulfides is typical (Figure 31) of the corrosion morphology at the scale/alloy interface. Behind this front of corrosion is a large region consisting mostly of oxide inclusions rich in both aluminum and iron. This indicates the possibility of a spinel-type

composition. Figure 31c shows from the sulfur map that some of the sulfide inclusions behind the distinct sulfide region were not yet oxidized. The implication is that this involves a sequential process rather than a parallel process, i.e., first the internal alloy must be sulfidized before it can be oxidized. Such a structure was not observed with the $CaSO_4$-char.

B. Effects of Gas Composition on Corrosion

Since the alloys were not exposed to coal char at a P_{O_2} different from that determined by the C/CO equilibrium, the effect of gas composition on coal char-induced corrosion can only be speculated on. At an oxygen potential of 10^{-19} atmosphere (Table 6) at a temperature of 982°C, penetration into the Fe-10Al alloy was considerable, but no extensive scaling occurred. Extensive scaling did occur on both the Fe-10Al and Fe-10Al-5Cr alloys in the preliminary screening runs (Figures 4 and 14). During these experiments, the oxygen partial pressure was about 10^{-6} to 10^{-5} atmosphere in the argon. However, at the char/alloy interface, the amount of oxygen can be much lower than in the gas phase due to the presence of the porous layer. It is reasonable to assume, therefore, that the limits of the oxygen concentration at the alloy surface are determined by the P_{O_2} in the gas and by the C/CO equilibrium at the surface. As discussed in Chapter 1, eventually the carbon would be oxidized and the P_{O_2} at the alloy surface would rise to that present in the gas. This coincided with the massive growth of scale on the alloys and may, in fact, be responsible for it.

Such a phenomenon is corroborated by the lack of external scaling when the alloys were exposed to coal char and the P_{O_2} was held to less than 10^{-18} atmosphere. Although there was considerable penetration into the Fe-10Al alloy after both 50 and 100 hours exposure, the implication is that the oxygen partial pressure was insufficient to promote external growth of scale as in the screening experiments.

Exposure to $CaSO_4$-char at low P_{O_2}'s revealed a different behavior. Figure 21a shows the overall appearance of the massive scale formed at $P_{O_2} = 10^{-19}$ atmosphere and 982°C. Figure 24 shows the cross-section of this scale and the resulting two-phase structure of discrete Al-poor and Al-rich regions. At the same temperature and gas composition, exposure to FeS-char results in the formation of Al_2O_3 only (Figure 22). No internal penetration and no formation or deposit of external sulfides were observed. This indicates that the P_{O_2} was insufficient to promote internal attack.

When the P_{O_2} was raised to 10^{-15} atmosphere and the alloys exposed to the same synthetic char compositions, a reversal of the previous trend was observed. Attack by FeS-char was rapid and resulted not only in extensive internal penetration but also external scaling (Figure 28). As previously described, this external scale began to show the smooth, molten appearance observed in the screening runs (Figure 29a and 30a), and after only five hours exposure the external scale was predominantly FeO with some FeS needles remaining. Only the Fe-10Al alloy underwent major corrosion. Considerable scaling was observed with $CaSO_4$-char on both Fe-10Al and Fe-10Al-15Cr (Figure 26). It had a considerably different appearance from either attack by FeS-char or by $CaSO_4$-char at the lower P_{O_2}'s . The cross-

section of the Fe-10Al-15Cr alloy shows a smooth region of constant iron and aluminum composition surrounded by regions of very different compositions. It appears almost as if a portion of the alloy itself was lifted off the surface by iron oxide and Al_2O_3-regions underneath. Here no sulfur penetration was observed. It appears from this that corrosion by $CaSO_4$-char at the higher oxygen partial pressures provided by the CO/CO_2 equilibrium occurs by a different mechanism from either corrosion induced by FeS-char or by $CaSO_4$-char at the lower partial pressures.

C. Effects of Alloy Composition on Corrosion

It was observed both here and in the preliminary screening runs that the addition of chromium greatly enhanced the corrosion resistance of the iron-aluminum alloys. The reasons for this are not precisely clear, but it is speculated (27) that thermodynamically both aluminum and chromium serve as a getter for sulfur. This means that prior to the internal formation of FeS, both the aluminum and chromium must be sufficiently depleted by the formation Al_2S_3 and/or CrS or Cr_2S_3 to deplete the alloy of aluminum and chromium. This takes time, and the amount of time required for such depletion depends on the kinetics of formation of the respective sulfides.

It now becomes increasingly possible that two different mechanisms are responsible for the observed attack by $CaSO_4$-char at high P_{O_2}'s and that observed from $CaSO_4$-char at a low P_{O_2} and FeS-char at a high P_{O_2}. In one case, $CaSO_4$-char at low P_{O_2} and FeS-char at high P_{O_2}, no attack was observed on the Fe-10Al-15Cr alloy while in the other case, fairly extensive attack was observed on the chromium-containing

ternary. If the same mechanism was responsible for corrosion under all circumstances, the same relation between the extents of attack should have been observed for both the binary and the ternary.

Neither of the 310 stainless steels underwent serious attack. On cross-sectioning, no sulfide inclusions were observed. It is possible that the lack of internal attack was not due to gettering of the sulfur by chromium but rather to the greater relative protection of the alloy by a Cr_2O_3 layer than by an Al_2O_3 layer.

D. Summary and Conclusions

It is now apparent the FeS is the main corrosive agent in coal char. Two observed phenomena account for this: 1) the morphology of attack by FeS-char is very similar to that observed for coal char and 2) the relative magnitude of attack increases as the oxygen partial pressure increases. This is due to oxidation of the FeS via equation 3-2 rather than reduction of $CaSO_4$ (equation 3-1) which increases as the P_{O_2} decreases. The precise mechanism of the attack is uncertain, but some conclusions can be drawn. Assuming the appropriate conditions exist, the first step may be contact of FeS with the surface. The FeS is then oxidized to FeO . During this process, the FeS-FeO eutectic is formed, and if the operating temperature is sufficiently high, the eutectic will melt onto the surface. As oxidation increases, the increased surface contact area will offer a large region where the sulfur released by oxidation of the sulfide can penetrate the surface. Alloys that contain aluminum and chromium then begin to undergo the formation of internal sulfides. These sulfides can be oxidized, and the sulfur released for further

internal attack. The form the attack will take will depend on the P_{O_2} and the relative concentrations of aluminum and chromium in the alloys.

This is not to say that there will be no attack from $CaSO_4$. $CaSO_4$ has been reported in coal and coal chars and at low oxygen partial pressure ($\leq 10^{-18}$ atmosphere) can provide ample sulfur for internal attack. The observations from this work are that compared to FeS, $CaSO_4$ is a minor contributor to internal sulfidation of these alloys. Nonetheless, the mechanism of the attack by $CaSO_4$ is sufficiently different from that by FeS that protecting against one (i.e., by additions of chromium to the alloy) may not be sufficient to protect against attack by the other.

E. Suggestions for Future Work

Much more work needs to be done to elucidate the precise mechanism of attack by FeS. The conclusions from this investigation are not definitive. Short term tests combined with quantitative analysis of the corrosion morphologies will help to determine the mechanism. A theoretical model of corrosion in relation to diffusion through porous layers would be useful to correlate predicted with observed results.

As yet, no technique exists to determine the kinetics of attack by coal char. Conventional quartz-spring thermobalances cannot be used because of the presence of a solid reactant. The development of a similar technique would be an invaluable tool to study kinetics of solid phase-induced corrosion.

Finally, a study of the effect of pre-oxidation on the rates of corrosion will be useful. As discussed, Cr_2O_3 and Al_2O_3 layers

are used as protective barriers to corrosion, but no data are available on the effect that char can have on these layers. Such experiments would be relatively simple and would help to flesh out the skeletal knowledge currently available on coal-char induced corrosion.

Acknowledgements

The author wishes to express his gratitude to Professor John Newman for his continued guidance and moral support during the pursuit of this research. He wishes to thank Mr. Alan V. Levy, Director of the Erosion-Corrosion Research Group, for his encouragement and support.

The author is especially grateful to the following people for many invaluable technical discussions: Dr. D. B. Rao, Dr. John Stringer, Professor Wayne Worrell, Dr. V. Nagarajan, Professor Leo Brewer, and Professor Israel Cornet.

Many people contributed their services during the preparation of this work: Carol Eaton, Gloria Pelatowski, Linda Betters, Ed Elliott, Robert Miner, Jim Hanson, and most of all, Walter Toutolmin without whose continual assistance much of this work would not have been accomplished in time.

Finally, the author wishes to thank his parents, B. E. Gordon and Naomi Gordon, and Lorraine Meuleners who, more than anything, were friends in need.

This work was performed under a grant from the United States Department of Energy, Division of Basic Energy Sciences.

REFERENCES

(1) Dixi Lee Ray, "The Nation's Energy Future," WASH-1281, December 1973.

(2) David J. Rose, "Energy Policy in the U.S.," Scientific American, 230, 20 (1974)

(3) "How Large is the U.S. Energy Resource Bank?," Engineering and Mining Journal, 72-216, (April, 1974) McGraw-Hill.

(4) A. L. Hammond, W. A. Metz, T. H. Maugh III, Energy and the Future, AAAS (Wash., D.C.), 1973, Chapter 5.

(5) "Synthane Coal Gasification Pilot Plant," Bureau of Mines, EIS-AA-72-5175-F, August 1972.

(6) B. A. Gordon and V. Nagarajan, "Corrosion of Fe-10Al-Cr Alloys by Coal Char," LBL-6946, October 1977, sub. to Oxidation of Metals.

(7) S. Gasior, Pittsburgh Energy Research Center, private communication, May 1976.

(8) J. Stringer and D. P. Whittle, "High Temperature Oxidation and Corrosion of Metals and Alloys," Revs. Int. Htes. Temp. et Refrac., 14, 6 (1977).

(9) J. M. Quets and W. H. Dresher, "Thermochemistry of the Hot Corrosion of Superalloys," Jour. Materials JMLSA, 4, 583 (1969).

(10) Robert A. Rapp, "Proceedings of Workshop on Materials Problems and Research Opportunities in Coal Conversion," Vol. II, spons. by NSF and OCR, April 13-16, 1974, Columbus, Ohio, pp. 313-34,

(11) Per Kofstad, High Temperature Oxidation of Metals, John Wiley and Sons, New York, 1966, Chap. 3.

(12) H. J. Gluskoter, "Inorganic Sulfur in Coal," Energy Sources, 3, 125 (1977).

(13) A. McNab, "Proceedings of Workshop on Materials Problems and Research Opportunities in Coal Conversion," Vol. II, spons. by NSF and OCR, April 16-18, 1974, pp. 33-48.

(14) Per Kofstad, op. cit., pp. 106-110.

(15) Ibid., pg. 112.

(16) Ibid., pg. 57.

(17) A. G. Guy, Introduction to Materials Science, McGraw-Hill, New York, 1972, pp. 272-75.

(18) A. U. Seybolt, "Observations on the Fe-Cr-O System," J. Electrochem. Soc., 107, 147 (1960).

(19) I. Kvernes, M. Oliveira, and P. Koftstad, "High Temperature Oxidation of Fe-13Cr-XAl Alloys in Air/H_2O Vapor Mixtures," Corrosion Science, 17, 237 (1977).

(20) Kenneth Denbigh, The Principles of Chemical Equilibrium, 3rd ed., Cambridge Univ. Press, 1971, pp. 140-43.

(21) G. R. Belton and R. J. Fruehan, "Mass Spectrometric Determination of Activities in Fe-Cr-Ni Alloys," Met. Trans., 1, 781 (1970).

(22) S. W. Gilby and G. R. St. Pierre, "Equilibrium Vapor Compositions of Components for Fe-Cr-Ni Alloys at 1600°C," Trans. Met. Soc. AIML, 245, 1749 (1969).

(23) G. N. Lewis and M. Randall, Thermodynamics, 2nd ed. revised by K. Pitzer and L. Brewer, McGraw-Hill, New York, 1961, pp. 153-58.

(24) John Prausnitz, Molecular Thermodynamics of Fluid-Phase Equilibria, Prentice-Hall, 1969, Chap. 9.

(25) Robert Rapp, op. cit., pp. 313-34.

(26) Peter L. Hemmings and R. A. Perkins, "Thermodynamic Phase Stability Diagrams for the Analysis of Corrosion Reactions in Coal Gasification/Combination Atmospheres," Lockheed Missiles and Space Co., LMSC-D558238, prep. for Electric Power Research Institute, 1977.

(27) B. A. Gordon, W. Worrell and V. Nagarajan, "Thermodynamic Predictions of the Behavior of Fe-Cr-Al Alloys in Coal Gasifier Environments," LBL-7320, Dec. 1977, submitted to Oxidation of Metals.

(28) JANAF Thermochemical Tables, 2nd ed., NSRAS-NBS 37, 1971.

(29) W. E. Boggs, "High Temperature Oxidation Resistance of Fe-Si-Al Alloys," Oxidation of Metals, 10, 277 (1977).

This report was done with support from the Department of Energy. Any conclusions or opinions expressed in this report represent solely those of the author(s) and not necessarily those of The Regents of the University of California, the Lawrence Berkeley Laboratory or the Department of Energy.

TECHNICAL INFORMATION DEPARTMENT
LAWRENCE BERKELEY LABORATORY
UNIVERSITY OF CALIFORNIA
BERKELEY, CALIFORNIA 94720